CenSegNet: a generalist high-throughput deep learning framework for centrosome phenotyping at spatial and single-cell resolution in heterogeneous tissues

Jiaoqi Cheng[1,2,8], Keqiang Fan[2,3,8], Miles Bailey[1,2], Xin Du[4], Rajesh Jena[5], Costantinos Savva[6,7], Mengyang Gou[1,2], Ramsey Cutress[2,6], Stephen Beers[2,7*], Xiaohao Cai[2,3*] and Salah Elias[1,2,9*]

[1]School of Biological Sciences, University of Southampton, Southampton SO17 1BJ, UK

[2]Institute for Life Sciences, University of Southampton, Southampton SO17 1BJ, UK

[3]School of Electronics and Computer Science, University of Southampton, Southampton SO17 1BJ, UK

[4]The Cavendish Laboratory, Department of Physics, University of Cambridge, Cambridge, CB3 0FZ, UK

[5]Department of Oncology, Cambridge University Hospitals NHS Foundation Trust, Cambridge, UK, University of Cambridge, CB2 0QQ, UK

[6]University Hospital Southampton NHS Foundation Trust, Southampton, SO16 6YD, UK

[7]Centre for Cancer Immunology, School of Cancer Sciences, Faculty of Medicine, University of Southampton, Southampton, SO16 6YD, UK

[8]These authors contributed equally

[9]Lead contact

[*]Correspondence: s.a.beers@soton.ac.uk, x.cai@soton.ac.uk and s.k.elias@soton.ac.uk

Abstract

Centrosome amplification (CA) is a hallmark of epithelial cancers, yet its spatial complexity and phenotypic heterogeneity remain poorly resolved due to limitations in conventional image analysis. We present CenSegNet (Centrosome Segmentation Network), a modular deep learning framework for high-resolution, context-aware segmentation of centrosomes and epithelial architecture across diverse tissue types. Integrating a dual-branch architecture with uncertainty-guided refinement, CenSegNet achieves state-of-the-art performance and generalisability across both immunofluorescence and immunohistochemistry modalities, outperforming existing models in accuracy and morphological fidelity. Applied to tissue microarrays (TMAs) containing 911 breast cancer sample cores from 127 patients, CenSegNet enables the first large-scale, spatially resolved quantification of numerical and structural CA at single-cell resolution. These CA subtypes are mechanistically uncoupled, exhibiting distinct spatial distributions, age-dependent dynamics, and associations with histological tumour grade, hormone receptor status, genomic alterations, and nodal involvement. Discordant CA profiles at tumour margins are linked to local aggressiveness and stromal remodelling, underscoring their clinical relevance. To support broad adoption and reproducibility, CenSegNet is released as an open-source Python library. Together, our findings establish CenSegNet as a scalable, generalisable platform for spatially resolved centrosome phenotyping in intact tissues, enabling systematic dissection of the biology of this organelle and its dysregulation in cancer and other epithelial diseases.

Introduction

Centrosomes, composed of a pair of orthogonally arranged centrioles surrounded by pericentriolar material (PCM), function as the principal microtubule-organising centres (MTOCs) in animal cells. They play essential roles in diverse cellular processes, including vesicular trafficking, cell polarity, motility, ciliogenesis, and the assembly of a bipolar mitotic spindle during cell division[1, 2]. Centrosome number is tightly regulated, with duplication occurring once per cell cycle during S phase, ensuring the formation of the mitotic spindle and equal inheritance of chromosomes by daughter cells[3-5].

Centrosome amplification (CA) can lead to multipolar spindle formation, chromosomal missegregation, and aneuploidy[3, 6, 7]—a hallmark of cancer[3, 4, 7]. The hypothesis that CA-induced aneuploidy contributes to tumorigenesis was first proposed by Theodor Boveri over a century ago[8]. In recent years, CA has been documented in several solid tumours including breast, prostate, colon, ovarian, and pancreatic cancers[3, 7, 9-13], as well as haematological malignancies such as multiple myeloma, lymphomas, and leukaemias[14, 15]. While its role in tumour initiation remains debated[6, 9, 16-18], CA is consistently associated with aggressive disease features, including high-grade histology, poor prognosis, recurrence, and metastasis[3, 7, 9, 19]. Despite its clinical relevance, CA remains poorly characterised at scale due to the lack of robust, high-throughput tools capable of resolving centrosome phenotypes in complex tissue architecture.

Mechanistically, CA arises from both numerical and structural centrosome defects. Numerical amplification results from centriole overduplication, *de novo* centriole assembly, cytokinesis failure, mitotic slippage and cell–cell fusion[20-29]. Disruption of cell-cycle progression, such as prolonged G2 arrest, can trigger premature centriole disengagement and reduplication *via* PLK1 activation[30, 31]. Fragmentation of the PCM, driven by dysregulation of proteins such as pericentrin, γ-tubulin, PLK4, PLK1, and Aurora-A, also contributes to numerical CA[7, 32-34]. Structural CA, on the other hand, involves aberrant accumulation of PCM[4, 7, 9, 35, 36] or defects in centriole architecture[37-39]. Among these centriole architectural defects, over-elongation and fragmentation can lead to unstable centriole

67 structures and further overduplication[37], suggesting a mechanistic link between numerical and
68 structural centrosome aberrations. Yet, their differential contributions to cancer biology remain to be
69 determined.

70 Manual centrosome annotation remains the standard but is time-consuming, low-throughput, and
71 prone to observer bias. Semi-automated pipelines have emerged to address these limitations. For
72 example, CenFind—a deep learning pipeline based on SpotNet—accurately detects and counts
73 centrioles in cultured cells using immunofluorescence images but does not support structural
74 phenotyping[40]. Other machine learning–based approaches have quantified centriole number and
75 linked supernumerary centrioles to PCM expansion in breast cancer cells[41]. Semi-automated
76 frameworks have also been developed for centrosome quantification in human breast histological
77 sections, including a HistoQuest-aided method detecting structural CA[42] and an IMARIS-based
78 pipeline integrating both structural and numerical CA[7, 43]. Similarly, a 3D imaging-based pipeline
79 quantified structural centriole abnormalities across cancer types[37]. However, these approaches
80 require manual curation and offer only moderate throughput. A recent high-throughput platform using
81 a Harmony™ software-based framework revealed heterogeneous CA phenotypes in ovarian cancer
82 tissues[44], yet lacked single-cell resolution and subtype discrimination. Moreover, most existing tools
83 are tailored to immunofluorescence imaging and are not compatible with standard chromogenic
84 immunohistochemistry workflows used in clinical pathology, limiting their diagnosis and translational
85 utility.

86 To address these limitations, we developed CenSegNet (Centrosome Segmentation Network), a
87 versatile deep learning framework for fully automated, pixel-level detection and segmentation of
88 centrosomes in both immunohistochemistry and immunofluorescence images at single-cell
89 resolution. CenSegNet integrates three state-of-the-art models: Ultralytics YOLOv11, a recent
90 evolution of the You Only Look Once family optimised for fast and accurate performance[45], U-Net,
91 an encoder–decoder convolutional network designed for precise pixel-wise segmentation[46], and
92 StarDist for shape-aware instance segmentation pipeline that models objects as star-convex

polygons to improve instance separation in dense cellular contexts[47], enabling robust delineation of epithelial cell boundaries within histopathological specimens. This systematically engineered architecture supports multiscale analysis of centrosomal features in morphologically complex tissue environments. We present a publicly accessible, expert-annotated dataset comprising human and murine breast tissues and human mammary epithelial cell cultures (MECs). Implemented in Python 3.10 with a PyQt5-based graphical interface, CenSegNet enables streamlined data input, real-time PyTorch-based inference, and modular extensibility. Benchmarking against expert annotations and alternative models, CenSegNet achieves pathologist-level accuracy across imaging modalities. Using CenSegNet, we perform the first high throughput, spatially resolved quantification of numerical and structural CA in clinical breast carcinomas. Our analyses reveal that these CA subtypes are mechanistically uncoupled and evolve along orthogonal spatial gradients: numerical CA predominates in proliferative tumour cores, whereas structural CA accumulates at invasive margins, reflecting distinct evolutionary pressures and microenvironmental cues. These spatial trajectories correlate with histological grade, hormone receptor status, HER2 expression, nodal involvement, and germline alterations, underscoring the role of centrosome dysregulation in driving intratumoral heterogeneity and progression. Importantly, we validated CenSegNet in other human epithelial tissues including kidney, colon, and appendix, demonstrating its generalisability and potential for broad application in spatial pathology and organelle-level phenotyping across diverse healthy and disease tissue contexts. To support widespread adoption, CenSegNet is released as an open-source Python library, available at https://github.com/SKELab/CenSegNet/ and https://zenodo.org/records/17131573.

Results

Development of CenSegNet for robust centrosome segmentation across imaging modalities

We generated tissue microarrays (TMAs) comprising 911 breast tissue cores from normal breast tissue, breast tumours, and adjacent areas, sampled from 127 patients enrolled in the ethically approved and clinically well-characterised BeGIN cohort (Investigating Outcomes from Breast Cancer: Correlating Genetic, Immunological and Nutritional Predictors), from University Hospital Southampton (UHS) (**Fig. 1a**; see Methods). Immunohistochemistry was performed using pericentrin antibody to label centrosomes, with haematoxylin counterstaining for nuclei (**Fig. 1a**). For training dataset construction, we manually annotated 14,679 centrosomes within 2,486 epithelial and 108 stromal compartments across 108 selected images (**Fig. 1a,** see Methods). To complement this, immunofluorescence was performed on human MECs and mouse mammary epithelium, labelling pericentrin and GT335 (centriole), with DAPI as nuclear counterstain. From this, an immunofluorescence training dataset was assembled comprising 1,285 annotated centrosomes from 143 cells from mouse tissue and 841 human MECs, revealing strong segmentation concordance between pericentrin and GT335 labelling [mouse tissue: R^2 = 0.9954; human MECs: R^2 = 0.9666 (MCF10A), 0.9085 (MCF10A-PLK4)] (**Fig. 1b, Supplementary Fig. 1a–f**).

Using these datasets, we initially benchmarked established segmentation models. U-Net, an encoder–decoder convolutional neural network optimised for pixel-wise segmentation[46], was selected for its extensive use in biomedical imaging. In our datasets, U-Net detected 82.98% of centrosomes in immunohistochemistry images and 97.6% in immunofluorescence, but despite achieving an overall F1 score of 0.85 in immunofluorescence, often the model either under-predicted or over-predicted centrosomes (**Supplementary Fig. 2a, b**). We next evaluated SegNet (**Fig. 1c**), another encoder-decoder model leveraging max-pooling indices for efficient upsampling[48]. It achieved 72.73% and 85% detection in immunohistochemistry and immunofluorescence, respectively, with a precision of 0.90 but reduced recall (0.75) in immunofluorescence and a

suboptimal overall F1 score of 0.68 in immunohistochemistry (0.82 in immunofluorescence) (**Supplementary Fig. 2c, d**). We also evaluated DeepLabv3+, a semantic segmentation model utilising atrous convolutions and atrous spatial pyramid pooling for multi-scale contextual information[49]. Despite its proven success in complex image domains, DeepLabv3+ achieved only 63.25% and 75.1% detection rates in immunohistochemistry and immunofluorescence, respectively (**Supplementary Fig. 2e, f**). These findings highlight the limitations of conventional segmentation pipelines when applied to structurally heterogeneous tissues.

To overcome these constraints, we developed CenSegNet, a novel modular framework that integrates object robust detection and segmentation (**Fig. 1c**). Rather than relying on whole-slide segmentation, CenSegNet focuses on single-cell regions while modelling the entire ROI, explicitly integrating object detection with region-based segmentation in a three-step architecture (**Fig. 1c**). This design enables a more comprehensive capture of centrosome spatial distributions and morphological features, addressing key challenges such as occlusion, small object detection, and the disambiguation of overlapping structures. The framework, first employs YOLOv11[45], a state-of-the-art object detection model, to identify potential centrosome candidates. YOLOv11 comprises a convolutional backbone for feature extraction, a neck for multi-scale aggregation, and a head for classification and localisation. We fine-tuned YOLOv11-seg[45, 50], a segmentation-optimised variant to further enhance detection accuracy, and applied a range of data augmentations—including hue, saturation, and value (HSV) adjustments, as well as geometric transformations such as translation, scaling, shearing, and horizontal flipping—to enhance generalisability (**Fig. 1c**; see Methods). To refine segmentation, we integrated U-Net in the second step. For all detected centrosomes, we extracted centrosome-centred patches (256 × 256 pixels, with 40-pixel padding) as input to a U-Net skip-connected encoder-decoder architecture for precise delineation. These patches underwent similar augmentation strategies as in the detection step, ensuring consistency. To accurately quantify centrosome numbers per cell, we incorporated StarDist[47] in the third step, a deep learning based instance segmentation tool widely adopted for nuclear and cell boundary segmentation in biomedical

167 imaging (**Fig. 1c**). In our immunohistochemistry datasets, StarDist segmented 764,354 cells
168 (**Supplementary Fig. 1g, h**). To validate StarDist-aided cell-level centrosome assignment in
169 complex tissues, we analysed keratin 8 (KRT8)-labelled mouse immunofluorescence (620 cells) and
170 human immunohistochemistry (620 cells) tissues. StarDist-based segmentation demonstrated
171 strong concordance with KRT8 (immunofluorescence: R^2 = 0.99; immunohistochemistry: R^2 =
172 0.9005) (see **Supplementary Fig. 1e-i**).

173 Collectively, these results demonstrate that CenSegNet's multistep architecture effectively
174 overcomes the limitations of conventional segmentation approaches, delivering robust,
175 generalisable centrosome detection and quantification across diverse imaging modalities and
176 complex tissue contexts.

177

178 **Validation of CenSegNet for scalable and high-precision centrosome segmentation**

179 To evaluate CenSegNet's performance, we compiled independent test datasets of 25
180 immunohistochemistry TMA cores and 17 immunofluorescence images. Predicted centrosome
181 counts were compared to manually annotated ground truth, revealing strong correlations in both
182 immunohistochemistry (R^2 = 0.9999) and immunofluorescence (R^2 = 0.9873) (**Fig. 2a–c**).
183 CenSegNet consistently outperformed U-Net, SegNet, and DeepLabv3+ in segmentation accuracy
184 and boundary resolution across both modalities, with the YOLOv11 detection module significantly
185 enhancing overall performance (**Fig. 2a–c**). To further assess precision, we used an independently
186 annotated subset of 550 centrosomes from tumour regions in the immunohistochemistry test set.
187 Again, CenSegNet demonstrated superior pixel-level segmentation compared to all benchmarks
188 (**Fig. 2d**). F1 score analysis across modalities yielded a mean of 0.82 for CenSegNet, outperforming
189 U-Net (0.72), SegNet (0.68), and DeepLabv3+ (0.65) (**Fig. 2a–e**). We next benchmarked
190 performance on 6,475 expert-annotated centrosomes—921 from normal tissue, 2,694 from edge
191 regions, and 2,860 from tumour cores (**Fig. 2f**). These annotations, stratified by size (0.5–1.0 μm^2 to
192 >10.5 μm^2), were compared with the full cohort of 333,148 automatically segmented centrosomes

193 (0–0.5 μm^2 to >12.0 μm^2)—10,834 from normal tissue, 91,803 from edge tissue, and 230,511 from
194 tumour tissue (**Fig. 2g**). Both datasets revealed similar size distributions, with the majority falling
195 within 2.0–3.0 μm^2 and a peak at 2.0–2.5 μm^2. Normal tissue showed a higher proportion of 1.0–2.0
196 μm^2 centrosomes, while edge regions had more large centrosomes than either normal or tumour
197 cores. Using a previously established threshold of 6.5 μm^2-size to define structural CA[42] (see
198 Methods), both datasets confirmed that centrosomes exceeding this size were absent in normal
199 tissue. Together, these results establish CenSegNet as a scalable, high-precision tool for
200 centrosome segmentation, with superior performance across image modalities, tissue
201 compartments, and size distributions—supporting its utility for high-throughput analysis in complex
202 tissue environments.
203
204 **CenSegNet enables spatial profiling of CA subtypes and clinical correlates in breast cancer**
205 To dissect the contribution of numerical (Num CA) and structural (Stru CA) CA in breast cancer, we
206 applied CenSegNet to multiplexed TMA data. Num CA and Stru CA were not correlated within either
207 tumour edge or core regions (**Supplementary Fig. 3a**), suggesting mechanistic independence. At
208 the single-cell level, increasing centrosome number per cell was associated with a reduction in the
209 size of individual centrosomes (**Supplementary Fig. 3b**), which become smaller, more uniform in
210 cells containing >4 centrosomes—implying a compensatory constraint on total centrosome volume.
211 These observations suggest that Stru CA and Num CA represent orthogonal axes of centrosome
212 dysregulation. In contrast, Num CA levels correlated positively between edge and tumour
213 compartments (R^2 = 0.4857; **Supplementary Fig. 3c**), indicating progressive numerical amplification
214 from tumour margins inward. This was reflected in an increasing proportion of cells with ≥4
215 centrosomes from normal tissue to the edge and tumour core (**Fig. 3a**). Stratifying patients into four
216 CA phenotypes ($Stru^-Num^-$, $Stru^+Num^+$, $Stru^+Num^-$, $Stru^-Num^+$) revealed that CA was widespread,
217 detected in 89.8% of edge and 95% of tumour regions (**Supplementary Fig. 3d**). Notably, 73% of
218 tumour regions exhibited both Stru CA and Num CA, representing a ~19.3% increase compared to

edge regions (**Supplementary Fig. 3d**). While the $Stru^{+}Num^{-}$ group accounted for 18.4% of edge regions but only 2% of tumour regions, the opposite trend was observed for the $Stru^{-}Num^{+}$ group (10.2% *versus* 20%, respectively). These findings allow us to conclude that structural and numerical centrosome aberrations are mechanistically uncoupled and highlight a spatial shift from centrosome enlargement at the tumour edge to centrosome accumulation in the tumour core.

To investigate how CA correlates with ages, we stratified patients into four groups: <50, 50–60, 60–70, >70 years. Num CA was elevated in patients aged 50–70 years across edge and tumour regions (**Fig. 3a, b**). The frequency of patients with detectable Num CA and Stru CA at the tumour edge markedly decreased in the 50–70 age group, resurging in patients over 70 years (**Fig. 3c**). Although fewer 50 to 60-year-old patients exhibited detectable CA at the edge, those that did had high levels of both CA subtypes (**Fig. 3d, e**). CA levels in tumour cores were relatively stable across age. Notably, normal tissues exhibited age-dependent increases in centrosome size, especially in patients over 70 (**Fig. 3f, g**), consistent with previous reports linking age to centrosome expansion *via* cumulative DNA damage[51]. In edge and tumour regions, centrosome size decreased between ages 50–70 before rising again in patients over 70 (**Fig. 3h, i**), while centrosome numbers followed the opposite trend, increasing in the 50–70 group before decreasing in the oldest cohort (**Fig. 3j**). This dynamic was mirrored by a higher proportion of cells with three centrosomes or more in the 50–60 age group (**Fig. 3k**). Finally, we did not observe significant differences in age distribution across the four CA-defined patient groups ($Stru^{-}Num^{-}$, $Stru^{+}Num^{+}$, $Stru^{+}Num^{-}$, and $Stru^{-}Num^{+}$) (**Supplementary Fig. 4a**). Thus, while age alone may not initiate CA in breast cancer, it modulates its spatial distribution and severity—particularly by promoting numerical amplification in the 50–70 age group and structural amplification in patients over 70.

We next evaluated associations between CA subtypes and clinicopathological features. Tumours lacking CA ($Stru^{-}Num^{-}$) displayed smaller total and invasive areas in the tumour core relative to the edge (**Supplementary Fig. 4b, c**), a pattern absent in other CA groups. Structural and numerical

244 CA prevalence increased with histological grade and nodal involvement (**Fig. 4a, b**). Stru CA was
245 inversely associated with tumour size across tumour (T) stages both edge and tumour regions, while
246 Num CA displayed region-specific variation (**Fig. 4c**). Stru CA and Num CA were more frequent at
247 the edge in invasive ductal carcinoma, but more abundant in the core of mixed-subtype tumours
248 (**Fig. 4d**). To further assess CA heterogeneity, patients were classified by composite CA defects into
249 $Stru^{high}Num^{high}$, $Stru^{high}Num^{low}$, $Stru^{low}Num^{low}$, $Stru^{low}Num^{high}$ CA groups (**Fig. 4e, f**). CA burden was
250 not age-associated (**Fig. 4g**), and distinct CA subtypes were linked to tumour behaviour. At the edge,
251 $Stru^{high}Num^{low}$ and $Stru^{low}Num^{high}$ CA tumours were associated with greater nodal involvement than
252 either the $Stru^{high}Num^{low}$ or $Stru^{low}Num^{high}$ CA groups (**Fig. 4h**), whereas no such differences were
253 observed across CA groups in the tumour core. $Stru^{low}Num^{high}$ CA tumours exhibited the smallest
254 overall size, while the largest tumours were enriched in $Stru^{high}Num^{low}$ (edge) and $Stru^{high}Num^{high}$
255 (tumour) CA groups (**Fig. 4i, j**). $Stru^{high}Num^{low}$ CA tumours grew more aggressively at the edge, while
256 $Stru^{high}Num^{high}$ CA tumours expanded predominantly in the core (**Fig. 4k**). While $Stru^{low}Num^{low}$ CA
257 was the most frequent subtype among large tumours across both regions, neither Num CA (in tumour
258 cores) nor Stru CA (at the edge) alone stratified tumour size (**Fig. 4l**). About 40% of tumours within
259 the $Stru^{high}Num^{high}$ CA group exhibited nodal involvement greater than N1 in the core (**Fig. 4m**),
260 consistent with increased metastatic potential. Many tumours with $Stru^{low}Num^{low}$ CA status at the
261 edge required nodal clearance, suggesting local aggressiveness independently of global CA burden
262 (**Fig. 4n**). Identified germline variants were exclusively observed in the $Stru^{high}Num^{high}$ CA group (**Fig.
263 4o**), consistent with associations between CA and BRCA1-driven genomic instability[52]. We also
264 evaluated the relationship between CA subtypes and body composition. Tumours with $Stru^{low}Num^{high}$
265 CA in the core were associated with increased fat-free mass index (FFMI), (**Supplementary Fig.
266 5a**), while fat mass index (FMI), waist circumference, and weight showed no differences across
267 groups or regions (**Supplementary Fig. 5b-d**). Taller patients more frequently exhibited
268 $Stru^{low}Num^{low}$ CA status in the edge regions, though this association was not observed in cores
269 (**Supplementary Fig. 5e**). Collectively, these findings indicate that spatial patterns of CA are linked

270 to tumour clinical parameters. Stru^{high}Num^{high} CA tumours define a high-risk subgroup marked by
271 large size, nodal spread, and genomic alterations, while Stru^{low}Num^{low} CA tumours—despite low CA
272 burden—can display local aggressiveness.

273 Single-cell analyses revealed further divergent CA subtype dynamics. At the edge regions, Num CA
274 decreased with increasing tumour size (**Supplementary Fig. 6a**), while Stru CA was enriched in
275 poorly differentiated but smaller tumours (**Supplementary Fig. 6b**). In the core, the proportion of
276 cells harbouring either CA subtype increased with both total and invasive tumour size
277 (**Supplementary Fig. 6c, d**). Num CA showed no significant differences across histological tumour
278 grades, although it was more prevalent in well-differentiated tumours (**Supplementary Fig. 6c**). Stru
279 CA levels were enriched in poorly differentiated tumours (**Supplementary Fig. 6d**). No significant
280 subtype-specific CA differences were observed across histological subtypes (**Supplementary Fig.
281 6a-d**), but cells from mixed tumours harboured more centrosomes in both compartments
282 (**Supplementary Fig. 7**), highlighting elevated Num CA as linked to increased tumour heterogeneity.
283 Together, these findings indicate a dynamic evolution of CA during tumour progression, with early-
284 stage tumours characterised by numerical defects and advanced tumours accumulating structural
285 abnormalities.

286 Finally, we explored CA patterns in the context of hormone receptor status, a key clinical determinant
287 in breast cancer[53, 54]. Stru CA levels varied by receptor status in both edge and tumour core
288 compartments (**Supplementary Fig. 8a**). HER2^{-} tumours had the highest Stru CA at the edge, while
289 PR^{-} and ER^{-} tumours had the lowest. In contrast, ER^{-} tumours displayed elevated Stru CA in the
290 core, with HER2^{+} tumours showing the lowest levels. Num CA also showed compartment-specific
291 trends: HER2^{+} tumours exhibited high Num CA at the edge but low levels in the core; ER^{-} tumours
292 showed the inverse pattern (**Supplementary Fig. 8b**). Despite broadly similar spatial trends
293 between Stru CA and Num CA across receptor-defined subtypes, HER2^{+} tumours emerged as an
294 exception (**Supplementary Fig. 8c, d**). HER2^{moderate} (2+) tumours had significantly lower Num CA

295 levels than HER2^{high} (3+) tumours in both compartments (**Supplementary Fig. 8e**), suggesting
296 HER2 dosage impacts centrosome number. HER2^{+} tumours were overrepresented in discordant CA
297 phenotypes—Stru^{low}Num^{high} (28.6%) and Stru^{high}Num^{low} (35.7%)—at the edge (**Supplementary Fig.**
298 **8f**), indicating HER2 may differentially regulate centrosome structure and number depending on
299 spatial context. This distribution was not observed in the tumour core. These observations point to
300 spatially resolved, hormone receptor-specific influence of CA patterns, particularly via HER2
301 signalling, in a microenvironment-dependent manner.
302
303 **CenSegNet reveals CA patterns linked to tumour subtype and progression**
304 Using CenSegNet-derived spatial quantifications, we compared dynamic shifts in Stru CA and Num
305 CA between tumour edges and cores. Patients were classified based on whether each CA subtype
306 was more abundant in the tumour core (T>E) or at the edge (E>T). Baseline clinicopathological
307 features were similar between spatial groups (**Supplementary Fig. 9**). Stru CA$^{T>E}$ tumours were
308 associated with lobular histology (15.8%), lower histological tumour grade (26.3% grade 3), and
309 lower HER2^{+} prevalence (15.8%). In contrast, Stru CA$^{E>T}$ tumours more frequently displayed high
310 tumour grade morphology (59.1% grade 3), higher HER2^{+} status (immunohistochemistry 3+ or FISH-
311 confirmed) (31.8%), and higher differentiation (**Supplementary Fig. 10a, b**). Single-cell analysis
312 revealed that in both Stru CA spatial groups, Num CA–positive cells consistently contained more
313 centrosomes in the core than at the edge (**Fig. 5a, b**), indicating a conserved numerical asymmetry.
314 Num CA spatial prevalence was also associated with aggressiveness: Num CA$^{T>E}$ tumours were
315 more often grade 3 (40.6%), had greater nodal involvement (31.2%), and lower HER2^{+} frequency
316 (12.5%) compared with Num CA$^{E>T}$ tumours (28.6%, 7.1%, and 35.7%, respectively;
317 **Supplementary Fig. 10c, d**). Mixed histology was more common in Num CA$^{T>E}$ tumours (12.5%),
318 whereas Num CA$^{E>T}$ tumours were associated with lobular carcinomas (28.6% *versus* 6.3%), a
319 subtype typically linked to slower growth and smaller size. Across both Num CA$^{T>E}$ Num CA$^{E>T}$
320 groups, centrosomes were significantly larger at the edge than in the core. Notably, Num CA–positive

cells with larger centrosomes harboured fewer of them (**Fig. 5c, d**), revealing a robust inverse relationship between centrosome size and number across all spatial groups (**Fig. 5e**). These findings highlight distinct spatial CA patterns associated with tumour subtype and behaviour. Tumours displaying a shift from fewer, larger centrosomes at the periphery to smaller, more numerous centrosomes in the core exhibit features of increased aggressiveness. These spatial patterns, resolved through CenSegNet, provide a proxy for tumour heterogeneity and may reflect the evolutionary trajectory of CA during tumour progression.

CenSegNet integration and accessible deployment for high-throughput centrosome analysis

To support broad adoption and integration into diverse analytical workflows, we provide CenSegNet as both a lightweight application programming interface (API) and an interactive graphical user interface (GUI) (**Fig. 6a, b**). The GUI comprises three modules: a data upload panel for inputting whole-slide or high-resolution images; a prediction module for adjustable inference parameters including probability thresholds and region selection for optimised segmentation of centrosomes and epithelial compartments; and an export tool for structured outputs. Post-inference, users can retrieve per-cell pixel-resolved size estimates, spatial coordinates, and centrosome counts within tissue context (**Fig. 6b)**. The interface supports batch processing and accepts both immunohistochemistry and immunofluorescence formats. Benchmarking shows that CenSegNet processes a 6,000 × 6,000-pixel immunohistochemistry image or a 2,048 × 2,048-pixel immunofluorescence image in <1 min on standard GPUs, enabling rapid, scalable analysis across large datasets.

342 **Discussion**

343 We introduce CenSegNet, a modular deep learning framework for quantification of centrosomes in
344 epithelial tissues at spatial and single-cell resolution. Unlike previous approaches that treat
345 morphological analysis and segmentation as separate tasks, CenSegNet integrates centrosome
346 detection and phenotyping, nuclear localisation, and epithelial boundary inference into a unified,
347 multichannel pipeline. This enables context-aware segmentation of both structural (Stru CA) and
348 numerical (Num CA) abnormalities across diverse imaging modalities. CenSegNet outperforms
349 established models—including U-Net, SegNet, and DeepLabv3+—in accuracy, generalisability, and
350 morphological fidelity, particularly in densely packed or morphologically heterogeneous tissue
351 regions. The framework comprises three specialised modules: a YOLOv11-based detector trained
352 on over 15,000 annotated centrosomes for robust localisation; a U-Net model for precise
353 segmentation of centrosome area and morphology; and a StarDist-based cell segmentation module
354 optimised for delineating epithelial boundaries in complex tissue architectures. This modular
355 integration, coupled with uncertainty-aware postprocessing, enables systematic and standardised
356 phenotyping of CA subtypes at single-cell and spatial resolution. Applied to 911 sample cores from
357 127 patients, CenSegNet-based profiling of over 330,000 centrosomes reveals previously
358 uncharacterised spatial trajectories and clinical correlates of Stru CA and Num CA, uncovering their
359 mechanistic uncoupling, age-dependent modulation, and associations with tumour progression,
360 hormone receptor status, HER2 expression, and genomic alterations.

361 Computational tools have been developed previously for CA quantification in epithelial cells. A semi-
362 automated machine learning pipeline quantified PCM defects and numerical CA in
363 immunofluorescence images of normal and breast cancer cells[41], but the method offers limited
364 spatial resolution and required extensive manual curation. Another semi-automated approach linked
365 centrosome size and number to chromosomal instability in human breast cancer tissues[17], yet lacked
366 single-cell resolution and scalability. Another pipeline assessed centriole number and length,
367 revealing structural defects arising from fragmentation and ectopic procentriole formation[37], but

368 without spatially resolved quantification. An automated detection algorithm for high-throughput
369 mapping of CA in ovarian cancer tissues, identified heterogeneous CA phenotypes associated with
370 chromosomal instability and chemotherapy resistance[44]. However, this method did not distinguish
371 between structural and numerical CA or provide single-cell semantic segmentation. CenSegNet
372 addresses these limitations by integrating cellular, spatial, and clinical dimensions of CA across
373 large-scale tissue cohorts. In doing so, it offers new insights into centrosome biology and the
374 functional relevance of CA heterogeneity in breast cancer, with implications for risk stratification and
375 precision oncology. Beyond breast cancer, CenSegNet has demonstrated generalisability across
376 diverse epithelial tissues—including kidney, colon, and appendix—characterised by high stromal
377 content and architectural complexity (**Supplementary Fig. 11**). To facilitate broad adoption, we
378 provide CenSegNet as an open-source GUI enabling scalable extraction of structured, spatially
379 anchored centrosome metrics. This will allow researchers and clinicians, regardless of computational
380 expertise, to integrate centrosome profiling into histopathological and biomarker discovery
381 workflows. Thus, CenSegNet extends beyond methodological innovation to practical application,
382 accelerating systematic investigation of centrosome biology across anatomically and histologically
383 diverse tissues, and enabling the identification of CA-driven vulnerabilities with potential therapeutic
384 relevance.

385 Recent studies using a composite centrosome amplification score (CAS) that integrates both
386 numerical and structural abnormalities[7, 43], showed a progressive increase in CAS from normal
387 breast tissue to invasive carcinoma. However, it did not distinguish the individual contributions of
388 numerical and structural centrosome abnormalities. Our spatially resolved single-cell analysis
389 demonstrates that Num CA and Stru CA represent distinct phenotypic axes of centrosome
390 dysregulation. Although they frequently co-occur in tumour tissues, they are uncorrelated at both
391 tissue and single-cell levels and exhibit unique spatial distributions: Stru CA is enriched at tumour
392 edges, while Num CA predominates in tumour cores, suggesting that different regional pressures
393 drive centrosome overduplication *versus* structural enlargement. Single-cell data further uncover a

394 robust inverse relationship between centrosome number and size—cells with multiple centrosomes
395 tend to have smaller ones—indicating a compensatory constraint on total centrosome volume.
396 Consistent with this, centriole over-elongation can induce CA *via* fragmentation and ectopic
397 procentriole formation in breast cancer cells[37], yet not all centrioles within a cell exhibit these
398 changes, highlighting intra-cellular heterogeneity in elongation susceptibility. Collectively, these
399 findings support a model in which Num CA and Stru CA are mechanistically uncoupled, evolving
400 along orthogonal spatial gradients during tumour progression. This challenges the monolithic view
401 of CA and instead portrays it as a dynamic, regionally modulated process shaped by local
402 microenvironmental cues. The mechanistic decoupling of CA has important implications for
403 understanding its functional heterogeneity in cancer and underscores the need for spatially informed
404 biomarkers.

405 CenSegNet-based profiling reveals that aging exerts distinct and spatially patterned effects on Stru
406 CA and Num CA in breast cancer. Num CA peaks between ages 50 and 70—overlapping with the
407 menopausal transition and the most common window for breast cancer diagnosis[55-57]—whereas Stru
408 CA accumulates progressively after age 70, indicating a later-life trajectory of centrosome
409 architectural dysregulation. While CA overall increases with age—including in normal tissues—our
410 data suggest that age is not a deterministic initiator but rather a factor that modulates the magnitude
411 and spatial distribution of CA subtypes. In mid-life patients, Num CA is preferentially enriched in
412 tumour cores—regions typically characterised by high proliferation—whereas Stru CA in older
413 individuals extends more diffusely, often into tumour margins, likely reflecting age-associated
414 changes in epithelial architecture, tissue repair dynamics, and microenvironmental stress. A study in
415 prostate cancer has reported elevated CA in patients over 53 years of age[7]. CA increases with age,
416 in normal breast epithelial cells derived from individuals aged 20-80, treated with DNA damage-
417 inducing stimuli[51]. Chronic centrosome overduplication in aging mouse models of intestinal cancer
418 drives aneuploidy and spontaneous tumorigenesis, supporting a role for age-associated CA in early
419 malignant transformation[18]. Centrosome function deteriorates with age, evidenced by accumulation

420 of structural defects and impaired mitotic fidelity[58, 59]. Aging epithelial cells exhibit centrosome
421 fragmentation, aberrant centriole elongation, and altered PCM composition[59, 60], while broader
422 declines in DNA repair and chromosomal segregation fidelity likely contribute to a permissive
423 environment for CA[59]. Thus, aging tissues accumulating centrosome abnormalities, mitotic fidelity
424 defects, and weakened genomic surveillance, may be more vulnerable to CA-driven tumorigenesis.
425 Our study delineates the divergence of CA subtypes across the lifespan. The inverse scaling
426 between centrosome number and size supports the idea that Num CA and Stru CA act as
427 compensatory, rather than co-occurring, phenotypes. Notably, Stru CA in elderly patients is
428 frequently associated with hormone receptor–negative tumours, implicating centrosome structural
429 dysregulation in the biology of more aggressive or dedifferentiated late-life cancers. CA can induce
430 breast cancer cell dedifferentiation and intrinsically drive high-grade tumours[61]. Age remains a key
431 prognostic factor in breast cancer, influencing tumour subtype distribution, hormone receptor status,
432 and genomic instability[62, 63]. Together, these results establish the first clinically and spatially resolved
433 framework for understanding how aging modulates centrosome biology in human cancer. This
434 framework lays the foundation for developing age-stratified biomarkers and clarifies why specific CA
435 subtypes and their associated chromosomal instability may emerge more frequently or have greater
436 clinical impact at distinct stages of life.

437 The spatial heterogeneity of CA and its clinical relevance for cancer remain poorly defined[3, 7].
438 CenSegNet systematically maps Stru CA and Num CA across tumour compartments and stratifies
439 tumours into composite CA subtypes with distinct spatial, biological, and clinical profiles.
440 $Stru^{high}Num^{high}$ CA tumours are consistently associated with larger size, greater nodal involvement,
441 and germline genomic alterations. Elevated CA in both core and edge regions suggests a cellular
442 composition primed for proliferative expansion and invasive dissemination. $Stru^{low}Num^{low}$ CA
443 tumours often required nodal clearance, supporting evidence that even modest CA can drive
444 aggressive behaviour in permissive genomic contexts—particularly when p53 surveillance is
445 compromised[7, 18, 64]. CenSegNet also uncovers spatial discordance in CA subtypes, with

446 $Stru^{high}Num^{low}$ and $Stru^{low}Num^{high}$ CA profiles enriched at the invasive front. These spatial signatures
447 are associated with enhanced metastatic potential, consistent with models in which centrosome
448 abnormalities promote invasion through both cell-autonomous[65-67] and non-cell-autonomous[68-70]
449 mechanisms. Structural centrosome defects have been shown to drive cell extrusion, facilitating
450 invasion[67, 71]. Our findings corroborate longitudinal studies of tumour progression, such as in Barrett's
451 oesophagus, where CA appears early in premalignant lesions and expands with p53 loss[64],
452 supporting a role for CA in tumour initiation rather than as a mere by-product of transformation.
453 Similarly, CA was shown to increase from normal tissue to ductal carcinoma *in situ* (DCIS) to invasive
454 carcinoma, and to correlate with recurrence and poor prognosis[7, 61]. Finally, our observation that Stru
455 CA and Num CA spatial patterns are uncoupled from systemic physiological metrics reinforces CA
456 as a tumour-intrinsic hallmark. Together, these results advance our understanding of centrosome
457 biology in cancer and highlight the power of CenSegNet-driven integration of subcellular organelle
458 features into spatial pathology, with direct implications for clinical decision-making, prognostic
459 modelling, and therapeutic targeting.

460 By integrating CenSegNet-based centrosome phenotyping with spatially resolved hormone receptor
461 profiling, we uncover compartment-specific associations between CA subtypes and ER/HER2
462 expression. Num CA is selectively enriched in ER^- tumours within the tumour core, whereas $HER2^+$
463 tumours display lower Num CA in the core despite elevated levels at the tumour edge. This spatial
464 divergence suggests that hormone receptor signalling modulates centrosome number and structure
465 in a regionally distinct manner. These observations corroborate previous studies linking CA to
466 hormone receptor status and tumour aggressiveness[37, 42, 66, 72] and support the hypothesis that ER
467 loss promotes CA through transcriptional or post-translational dysregulation of centriole biogenesis
468 pathways. Basal-like $ER^-PR^-HER2^-$ breast cancers—characterised by genomic instability and poor
469 prognosis[73], frequently exhibit high CA, often with centriole fragmentation and ectopic procentriole
470 formation driven by over-elongation[37]. These defects recruit excess pericentriolar material (PCM),
471 generating supernumerary or structurally abnormal MTOCs that drive mitotic errors and

472 chromosomal instability[74, 75]. In contrast, HER2^{+} tumours are more frequently enriched in discordant
473 CA subtypes (Stru^{low}Num^{high} and Stru^{high}Num^{low}) at the tumour edge, suggesting that HER2 signalling
474 may differentially regulate centrosome number and structure depending on spatial context. This is
475 consistent with evidence that both PLK4 and AURKA expression—key regulators of centriole
476 biogenesis and maturation, respectively—is differentially influenced by HER2 status[72, 76]. Despite
477 high proliferative capacity, HER2^{+} tumours exhibit lower overall CA, raising the possibility that these
478 tumours suppress CA to preserve mitotic fidelity or evade immune detection. Together, our findings
479 identify spatially distinct and mechanistically diverse relationships between hormone receptor
480 signalling and centrosome biology. ER loss is associated with elevated Num CA and mitotic instability
481 in tumour cores, while HER2 signalling appears to exert compartmentalised control over CA subtype
482 distribution. Spatially resolved centrosome profiling thus provides a framework for identifying
483 hormone-specific vulnerabilities that could inform targeted breast cancer therapies.

484 CenSegNet enables fine-grained stratification of tumours based on the relative abundance of
485 structural (Stru CA) and numerical (Num CA) centrosome abnormalities, revealing distinct spatial–
486 biological associations. Tumours with Stru CA enriched at the invasive edge (Stru CA$^{E>T}$) are more
487 proliferative, more frequently HER2^{+}, and exhibit higher differentiation, whereas those with Stru CA
488 more abundant in the core (Stru CA$^{T>E}$) are more commonly associated with lobular histology and
489 slower growth. Single-cell analyses further show that tumours with grade 3 histology, nodal
490 involvement, and mixed subtypes—hallmarks of aggressive disease—are more prevalent in the Num
491 CA$^{T>E}$ subgroup, while Num CA$^{E>T}$ tumours are enriched for lobular carcinomas, typically linked to
492 indolent behaviour[73]. These spatially resolved patterns corroborate previous reports suggesting that
493 numerical centrosome abnormalities increase with tumour progression and are more frequent in
494 aggressive basal-like carcinomas[7, 37]. Our single-cell data also reveal an inverse relationship
495 between centrosome number and size—where edge regions harbour fewer but larger
496 centrosomes—supporting a model in which Stru CA at the periphery primes cells to acquire invasive
497 behaviours, while Num CA in the core drives proliferation and genomic instability. This dynamic

interplay likely reflects microenvironmental influences on CA trajectories during tumour progression. These findings extend the “CA set point” concept[77], which postulates that tumours maintain a context-dependent equilibrium of CA phenotypes to balance proliferation, invasion and survival. CenSegNet-based spatial profiling demonstrates that CA is not only subtype-specific but also spatially regulated, providing new insights into the architectural evolution and heterogeneity of breast cancer.

In summary, CenSegNet delivers the first fully integrated and spatially resolved framework for profiling CA at single-cell resolution across large-scale human cancer tissues. By enabling precise, high-throughput quantification of both numerical and structural CA phenotypes, CenSegNet uncovers distinct mechanistic, temporal, and spatial trajectories of centrosome dysregulation in breast cancer. The discovery that numerical and structural CA are decoupled numerical and structural CA are decoupled—not only in cellular architecture but also in their associations with clinical features such as tumour grade, hormone receptor status, germline mutation, and patient age—advances our understanding of how centrosome abnormalities contribute to intratumoral heterogeneity, tumour progression, with considerable implications for therapeutic resistance. Importantly, the identification of compensatory dynamics between centrosome number and size, and their divergent distributions across tumour cores and margins, points to context-specific roles in modulating local tumour ecology and genomic instability. These insights challenge the longstanding view of CA as a uniform driver of malignancy, instead positioning CA subtypes as distinct functional modules in tumour evolution. CenSegNet thus provides a foundation for developing CA-based biomarkers to stratify patients by tumour subtype, age, and aggressiveness, and opens opportunities for therapies targeting CA-driven vulnerabilities. Given the availability of PLK4, AURKA, and HSET inhibitors[78-82], spatial CA maps could guide personalised strategies, particularly in tumours with discordant amplification phenotypes. Future studies integrating CenSegNet-based CA profiling with transcriptomic and proteomic analyses will be essential to uncover the molecular drivers of spatial

523 CA dynamics and clarify their roles in tumour progression, metastatic dissemination, and therapy
524 resistance.

525 **Methods**

526

527 **Ethics and human breast tissues**

528 The study participants were a subgroup of women diagnosed with early breast cancer who were
529 recruited to a single-centre prospective observational cohort study at University Hospitals
530 Southampton, "Investigating Outcomes from Breast Cancer: Correlating Genetic, Immunological and
531 Nutritional Predictors (BeGIN)[83, 84]." All procedures performed in studies involving human participants
532 were in accordance with the ethical standards of the institutional and/or national research committee
533 and with the 1964 Helsinki declaration and its later amendments or comparable ethical standards.
534 All participants in BeGIN gave written informed consent. The research ethics committee approved
535 the study (Research Ethics Committee (REC) - Cambridgeshire and Hertfordshire reference number:
536 14/EE/1297). Women were eligible for the BeGIN study if they were aged >18 years and diagnosed
537 with invasive breast cancer or DCIS at University Hospital Southampton after May 2015. Linked
538 anonymised patient information, including patient characteristics, tumour characteristics and clinical
539 management, were extracted from the hospital electronic record system. Body composition
540 parameters were measured using Bioelectrical Impedance Analysis (BIA) with a phase-sensitive, 8-
541 electrode device (Seca mBCA515)[85]. To conduct this study, 911 cores from 127 breast cancer
542 patients were used. The TMAs were constructed from formalin fixed paraffin embedded (FFPE)
543 histopathology tissue blocks from surgical treatment surplus to diagnostic requirements. Colon,
544 kidney, and appendix tissue were incorporated into breast tissue TMAs to facilitate orientation during
545 sectioning and analysis. Colon and kidney samples consisted of histologically normal tissue, the
546 status of which was independently verified by a board-certified pathologist. A summary of the
547 clinicopathological information linked to the human breast samples used in this study is included in
548 **Supplementary Table 1**. Anonymous data from the BeGIN study is available for request to
549 researchers who provide a completed Data Sharing request form that describes a methodologically
550 sound proposal, for the purpose of the approved proposal. Proposals will be reviewed by the study

551 steering committee. Data will be shared once all parties have signed relevant data sharing
552 documentation, covering the study steering committee conditions for sharing and if required, an
553 additional Data Sharing Agreement from the Sponsor.
554
555 **Ethics and mice**
556 BALB/c HER-2/neu transgenic mice (referred to as BALB-NeuT)[86] carrying the transforming rat *Her-*
557 *2/neu* oncogene under control of a MMTV-LTR were used. All experimental procedures involving
558 mice were approved by the University of Southampton Local Ethics Committee and registered with
559 the Ethics and Research Governance Online II (ERGO II; ID: 65385). All animal work was conducted
560 in accordance with UK Home Office regulations, adhering to the principles of the 3Rs (Replacement,
561 Reduction, Refinement) and the ARRIVE (Animal Research: Reporting of In Vivo Experiments)
562 guidelines to minimise animal suffering throughout the study. Mice were housed in a specific
563 pathogen-free (SPF) facility under controlled environmental conditions, including regulated
564 temperature and humidity, with a 12-hour light/dark cycle. Animals had ad libitum access to standard
565 chow and water.
566
567 **Cell culture**
568 MCF10A is a non-transformed human mammary epithelial cell line (ATCC® CRL-10317). The
569 MCF10A-PLK4 cell line is a genetically engineered derivative of MCF10A that enables inducible
570 overexpression of Polo-like kinase 4 (PLK4), a master regulator of centrosome duplication whose
571 upregulation induces centrosome amplification[66]. The MCF10A-PLK4 cell line was kindly provided
572 by Dr. Susana Godinho (The Barts Cancer Institute, Queen Mary University of London). Both
573 MCF10A and MCF10A-PLK4 cells were cultured in DMEM/F12 medium (Invitrogen), supplemented
574 with 10% donor horse serum (Gibco, 31331028), 20 ng/ml human epidermal growth factor (EGF;
575 Sigma, E9644), 10 µg/ml insulin (Sigma, I1882), 100 µg/ml hydrocortisone (Sigma, H0888), 1 ng/ml
576 cholera toxin (Sigma, C8052), and 50 U/ml penicillin with 50 µg/ml streptomycin (Life Technologies).

577 Cells were maintained at 37 °C in a humidified incubator with 5% CO_2. To induce PLK4
578 overexpression, cells were treated with doxycycline (Sigma, D9891) at 2 µg/ml for 48 hours.
579
580 **Tissue microarray construction and immunohistochemistry**
581 Tissue microarrays (TMAs) were constructed using formalin-fixed, paraffin-embedded (FFPE) tissue
582 samples obtained following breast cancer surgery from 127 patients diagnosed with primary invasive
583 breast carcinoma at University Hospital Southampton between July 9, 2015, and January 31, 2019,
584 and participating in the BeGIN study. All patients underwent standardised treatment at a single
585 institution, consisting of surgery, followed by adjuvant treatments according to local and national
586 protocols. Pathological evaluation of hormone receptor and HER2 expression was conducted
587 according to established national and international guidelines[87, 88]. Immunohistochemistry was used
588 to determine hormone receptor status, and in situ hybridization (ISH) was employed to confirm HER2
589 positivity for tumours with an IHC score of 2+. All procedures were performed within the standard
590 clinical diagnostic pathway. A total of 911 sample cores were systematically sampled from three
591 distinct, pathologically classified regions for each patient: tumour tissue (Tumour), tumour margin
592 (Edge), and tumour-free tissue (Normal). Each patient represented by three technical replicate cores
593 from Tumour, Edge, and Normal regions, were procured for analysis. Each 0.6 mm in diameter and
594 5 µm in thickness were extracted from formalin-fixed, paraffin-embedded specimens and arrayed
595 into recipient tissue microarray (TMA) blocks. This tri-regional, triplicate-core sampling strategy was
596 designed to provide a comprehensive and robust representation of the tissue heterogeneity within
597 and around the tumour microenvironment. TMA sections were mounted onto TOMO® adhesion
598 microscope slides. Immunohistochemistry was performed using the Dako Autostainer Link 48
599 automated platform. Endogenous peroxidase activity was quenched using EnVision FLEX blocking
600 reagent (Dako), followed by a 30-minute incubation with the primary antibody against pericentrin
601 (1:500 dilution; Abcam, ab4448). Signal amplification and enzymatic detection were achieved using
602 EnVision FLEX HRP (Dako, 20 minutes) and Rabbit Link (Dako, 15 minutes). Slides were

603 counterstained with haematoxylin following three 5-minute washes in 3-amino-9-ethylcarbazole
604 (AEC).
605
606 **Assessment of hormone receptor status**
607 ER or PR expression were evaluated by immunohistochemistry and scored using the Allred system
608 (range 0–8). Tumours with an Allred score ≥ 3 were classified as ER or PR positive. HER2 status
609 was determined by immunohistochemistry and scored as 0, 1+, 2+, or 3+. Tumours with a score of
610 3+ were classified as HER2 positive. Cases with a score of 2+ were considered equivocal were
611 further assessed by fluorescence in situ hybridization (FISH). Tumours with FISH amplification were
612 designed as HER2 positive, defined as a HER2/CEP17 ratio ≥ 2.0 or average HER2 copy number ≥
613 6.0 signals per cell.
614
615 **Immunofluorescence**
616 The following primary antibodies were used: anti-GT335 (1:800; Adipogen, AG-20B-0020-C100),
617 anti-pericentrin (1:250; Abcam, ab4448), and anti-keratin 8/18 (KRT8/18; 1:300; Origene, BP5007).
618 Secondary antibodies (Life Technologies) included goat anti-mouse (A-32723), anti-rabbit (A-11037
619 and A-11008), and anti-guinea pig (A-21450), each conjugated to Alexa Fluor 488, Alexa Fluor 594,
620 or Alexa Fluor 647, and used at a final concentration of 5 µg/ml.
621 OCT-embedded mammary gland sections (30 µm thick) from BALB-NeuT mice were cryosectioned,
622 air-dried for 30 minutes, and fixed in 4% paraformaldehyde (PFA) for 20 minutes at room
623 temperature. Sections were permeabilised for 45 minutes with 0.1% Triton X-100 in PBS, then
624 blocked for 2 hours in a solution containing 2% bovine serum albumin (BSA), 5% foetal bovine serum
625 (FBS; Gibco), and 0.1% Triton X-100 in PBS. Sections were incubated overnight at 4 °C with primary
626 antibodies against pericentrin, GT335, and KRT8, followed by washing and incubation with the
627 appropriate secondary antibodies for 2 hours at room temperature. Nuclei were counterstained with
628 DAPI using Fluoroshield mounting medium (Sigma, F6057).

629 MCF10A and MCF10A-PLK4 cells were fixed in anhydrous methanol at −20 °C for 10 minutes,
630 followed by permeabilisation with 0.1% Triton X-100 in PBS for 2 minutes. Cells were then washed
631 three times for 5 minutes each with 0.1% Triton X-100 in PBS. Blocking was performed using 3%
632 BSA in 0.1% Triton X-100 in PBS for 1 hour at room temperature. Cells were incubated overnight at
633 4 °C with primary antibodies against pericentrin and GT335. After washing, cells were incubated with
634 the appropriate secondary antibodies for 1 hour at room temperature and counterstained with DAPI
635 using Fluoroshield.
636
637 **Microscopy and image annotation**
638 Immunohistochemistry images were acquired using a Zeiss Axio Imager Z1 upright microscope
639 (Zeiss), equipped with an AxioCam MRc5 colour camera. Image capture was performed using Zeiss
640 ZEN imaging software, following a predefined whole-slide brightfield scanning protocol (Whole Slide
641 [WS] Brightfield [BF] fold-light) with a 20× objective lens. This configuration enabled high-resolution
642 imaging of tissue sections with consistent illumination and contrast across samples.

643 Immunofluorescence images were captured using an inverted Leica STELLARIS 5 laser scanning
644 confocal microscope (Leica Microsystems), equipped with a 40× oil immersion objective (HC PL
645 APO 40×/1.30 Oil CS2). Z-stacks were acquired at 16-bit depth with a 0.2 μm step size, using fields
646 of view (FOVs) ranging from 1024 × 1024 to 2048 × 2048 pixels. All cells from all FOVs obtained
647 during the experiments were included in the evaluation of model performance. Image processing
648 was performed using Fiji software (https://imagej.net/software/fiji/)[89].

649 Manual annotations were performed by Jiaoqi Cheng (see **Supplementary Fig. 12**), who received
650 training and supervision from Constantinos Savva. Centrosome size quantification in
651 immunohistochemistry images was performed using calibrated spatial resolution, wherein each pixel
652 corresponded to an area of 0.0483 μm^2. For each centrosome, pixel-level segmentation masks were
653 used to compute total pixel occupancy, which was then multiplied by the calibrated pixel area to
654 derive centrosome size in μm^2.

To generate the immunohistochemistry training dataset, images from 78 patients were included, comprising human breast cancer tissue, normal breast tissue, normal liver, and normal kidney samples. Within these images, annotations were made for centrosomes (n = 14,679), epithelial compartments (n = 2,486), and stromal compartments (n = 108), using QuPath v0.5.1 (https://qupath.github.io/)[90]. All centrosome annotations were performed under 200× magnification for each region of interest (ROI). The manual annotation process required over 200 person-hours. Annotations were exported as GeoJSON files.

For the immunofluorescence training dataset, only 15 high-resolution image z-stacks of MCF10A and MCF10A-PLK4 cell lines were required. Annotation was performed using Cellpose 3.0[91, 92]. Datasets were first maximum-intensity projected, then split into contrast-adjusted single-channel images, with boundaries defined by edge features visible in the blue channel. The manual annotation process took approximately 16 person-hours. All annotations were exported as SVG files.

Image processing and model training

Image processing. For immunohistochemistry image processing in the CenSegNet pipeline, raw microscopy images were pre-processed to enhance contrast and suppress background noise, thereby improving the visibility of cellular structures. Each image was cropped into overlapping patches of 256 × 256 pixels with a stride of 300 pixels. Patches exhibiting artefacts or poor quality were manually excluded to ensure dataset integrity. The final immunohistochemistry dataset comprised 1,122 annotated patches, each containing labelled information on centrosome location and size. For immunofluorescence images, RGB channels were converted to greyscale to reduce dimensionality and simplify the training process. This transformation allowed the model to remain invariant to colour information while improving computational efficiency.

Model architecture and training. CenSegNet employs a modular three-step architecture comprising approximately 40 million trainable parameters. The first step consists of a detection head that localises candidate ROIs, while the second stage performs fine-grained segmentation within

these ROIs to achieve precise spatial delineation. This decoupled design enables task-specific optimisation and improves memory efficiency and training stability. In the detection stage, we fine-tuned YOLOv11-seg model[45] (https://github.com/ultralytics/ultralytics) using our own training set, guided by a composite loss function comprising box loss, segmentation loss, classification loss, and distribution focal loss. These components respectively optimise object localisation, foreground-background separation, class prediction, and robustness to complex spatial distributions. Training was performed using the AdamW optimiser (learning rate = 0.002, momentum = 0.9) with a batch size of 16 over 300 epochs. The segmentation step 2 employed a U-Net architecture[46] with three input channels (RGB) and one output channel. Given the small size of centrosomes, segmentation was formulated as a binary classification task. The model was trained for 100 epochs using the Binary Cross Entropy with Logits loss function (BCEWithLogitsLoss). Optimisation was performed using RMSprop (learning rate = 1×10^{-4}, weight decay = 1×10^{-8}, momentum = 0.9), which stabilised training and improved convergence for small target structures. Training was conducted in Python (v3.10) using PyTorch (v2.1). We applied data augmentations, such as HSV colour jittering and geometric transformations, which can be easily implemented using the torchvision.transforms module in PyTorch. The detection head was trained independently for approximately 24 hours, followed by an additional 12 hours of training for the segmentation head. All experiments were run on four NVIDIA A100 GPUs (40 GB VRAM each) using PyTorch's Distributed Data Parallel (DDP) framework with NVIDIA Collective Communications Library (NCCL) backend for gradient synchronisation. Input batches were evenly partitioned across GPUs, with local gradient computation and synchronisation via NCCL's optimised collective communication, achieving near-linear scaling in throughput. Batch sizes were dynamically adjusted to maximise GPU utilisation while maintaining training stability.

Comparative segmentation models. To benchmark CenSegNet, we compared its performance against established segmentation models including U-Net[46], SegNet[48], and DeepLabv3+[49]. Each model was trained on uniformly sized 256 × 256 image patches cropped from the original dataset.

Official implementations were used without architectural modifications. Comparative experiments were conducted with and without ImageNet pretraining to assess the impact of transfer learning. Model outputs were evaluated against ground truth segmentation masks using a composite loss function combining weighted binary cross-entropy and Dice loss, balancing pixel-wise accuracy with regional overlap. All models were trained under identical conditions: Adam optimiser (initial learning rate = 1×10^{-4}), cosine learning rate decay, L2 regularisation (weight decay = 1×10^{-8}), batch size of 16, and early stopping based on validation loss plateauing. A total of 108 immunohistochemistry images were manually annotated and divided into training (n=80), validation (8), and test (n=20) datasets. An additional private dataset comprising 25 images was generated and manually curated for evaluation.

Cell segmentation. For cell nucleus segmentation step 3, we integrated StarDist[47] with the QuPath platform. StarDist offers state-of-the-art performance in dense and noisy biological environments. Following accurate nucleus segmentation, cell membrane boundaries were estimated using the spatial coordinates of nuclei as anchor points. Expansion thresholds of 3, 4, 5, and 6 μm were tested and validated against KRT8-stained images to determine the optimal value for our dataset.

Evaluation metrics

Centrosome segmentation performance. Centrosome segmentation performance was evaluated on a test set comprising 25 immunohistochemistry and 17 immunofluorescence images. Metrics included precision, recall, intersection over union (IoU), and F1 score. IoU was defined as the common area between the predicted segmentation and the ground truth:

$$IoU = \frac{|\text{Prediction} \cap \text{Groundtruth}|}{|\text{Prediction} \cup \text{Groundtruth}|}$$

The F1 score, representing the harmonic mean of precision and recall, was calculated as:

$$F1\ score = 2 * \frac{\text{Precision} * \text{Recall}}{\text{Precision} + \text{Recall}}$$

With:

$$Precision = \frac{\mathrm{TP}}{\mathrm{TP} + \mathrm{FP}}, \qquad Recall = \frac{TP}{\mathrm{TP} + \mathrm{FN}}$$

Where, TP, FP, and FN denote true positives, false positives, and false negatives, respectively. Both IoU and F1 scores range from 0 to 1, with higher values indicating superior segmentation performance.

These metrics provide a comprehensive assessment of spatial overlap, agreement, and pixel-wise accuracy, with higher values indicating better performance in medical image segmentation.

Epithelial segmentation performance. To assess the performance of epithelial segmentation by CenSegNet, we quantified the $F1^{IoU50}$ metric[93], a widely adopted benchmark in biomedical image analysis. IoU50 means the IoU threshold was set to 0.5 (or 50%). A predicted bounding box was considered a correct detection if: IoU with ground truth ≥0.5.

Statistical analysis

The exact n is stated in the corresponding figure legend. GraphPad Prism 10.3.1 (GraphPad Software) was used to perform statistical significance analysis. Normality and lognormality were assessed prior to statistical analysis. For datasets exhibiting a normal distribution, comparisons between two groups were conducted using an unpaired t-test, while comparisons across multiple groups were performed using one-way analysis of variance (ANOVA), followed by Tukey's post hoc test for multiple comparisons or two-way ANOVA, followed by Tukey's post hoc test for multiple comparisons. For datasets that deviated from normality, non-parametric testing was employed, using the Kruskal-Wallis test for multiple group comparisons, followed by the Mann-Whitney U test as a post hoc analysis. For correlation analysis, a two-tailed Pearson test was used followed by simple linear regression for graphical representation for correlation analysis. To compare the composition of groups based on categorical variables (e.g., histological tumour grade, T stage, histological tumour types, hormone status, nodal status, nodal clearance, HER2 status), Fisher's exact test was

employed. This non-parametric test was chosen for its appropriateness with count data and its ability to provide accurate p-values when expected cell counts are low (<5). All comparisons were two-sided. All values were presented as mean ± s.e.m. For all statistical tests, $^{*}P \leq 0.05$, $^{**}P \leq 0.01$, $^{***}P \leq 0.001$ and $^{****}P \leq 0.0001$ were considered significant.

Assistance with manuscript preparation

During the preparation of this manuscript, ChatGPT (OpenAI, version 4) was used to assist with stylistic and grammatical refinement. All AI-generated content was critically reviewed and edited by the authors, who take full responsibility for its accuracy and integrity.

766 **Data availability**

767 Examples of immunohistochemistry and immunofluorescence image datasets used for
768 benchmarking and for testing CenSegNet within the demo version of the pipeline are available on
769 https://github.com/SKELab/CenSegNet/ and https://zenodo.org/records/17131573. All other
770 relevant data supporting the key findings of this study are available within the article and its
771 Supplementary Information files or upon reasonable request. A summary of the human breast
772 samples used in this study are included in Supplementary Table 1. For participants on the BeGIN
773 study, further donor anonymised clinicopathological information is available upon reasonable
774 request, provided all relevant ethics approvals are in place (see "Ethics and human breast tissues"
775 section for further details). The source data that support the findings in all Figures and
776 Supplementary Figures are provided as a Source Data file within the paper. All reagents generated
777 in this study are available upon reasonable request.

778

779 **Code availability**

780 The source code and software CenSegNet as a ready-to-use executable with a quickstart guide,
781 example datasets and step-by-step procedures are freely available at
782 https://github.com/SKELab/CenSegNet/ and https://zenodo.org/records/17131573.

783 .

784

785 **Acknowledgements**

786 We would like to thank Dr. Mark Willett at the Imaging and Microscopy Centre for valuable assistance
787 with fluorescence microscopy; Monette Lopez at the Research Histology Facility, University Hospital
788 Southampton for performing immunohistochemistry staining and imaging; Dr Margaret Ashton-Key
789 for classifying breast tumour compartments (normal, edge, core) and providing advice on
790 immunohistochemistry staining conditions; Professor Susana Godinho for providing the MCF10A
791 and MCF10A-PLK4 cell lines. In addition, we thank Dr. Xi Jia, Dr. Colinda Scheele, Dr. Marcin
792 Przewloka, and Dr. Kif Liakath-Ali, for critically reviewing the manuscript. Cartoons in Figs. 1a, 1c
793 and Supplementary Fig. 12 were created using https://www.freepik.com/. This work was supported
794 by an MRC New Investigator Research Grant (MR/R026610/1) awarded to S.E. and an Institute for
795 Life Sciences Pilot Grant awarded to R.C., S.B. and S.E. JC was supported by the Gerald Kerkut
796 Charitable Trust and a China Scholarship Council (CSC) PhD studentship. The BeGIN study was
797 supported by Breast Cancer Now.

Author contributions

J.C. designed and performed experiments, analysed, interpreted the data, and wrote the manuscript. K.F. trained models and developed CenSegNet. C.S. M.B and X.D. supervised centrosome annotation and performed transfer annotations from GeoJSON Files to PNG files and data analysis. M.G. performed immunofluorescence experiments. R.C. provided ethically approved BeGIN breast cancer tissues. S.B. supervised J.C. and interpreted the data. X.C. supervised K.F. on CenSegNet development. S.E. conceived and designed the project, analysed and interpreted the data, supervised J.C., wrote the manuscript, and acquired funding. All the authors provided intellectual input, edited, and approved the final manuscript.

807 **Competing interests**

808 C.S. reports involvement in a research collaboration with Proteotype and BioNTech. R.C. reports the
809 following declaration: 1. Grants or Contracts: AstraZeneca, awarded an educational grant to the
810 University of Southampton in November 2021 for the long-term follow-up of the POSH study. 2.
811 Leadership or Fiduciary Roles: NICE, acts as a Breast Cancer Topic Advisor, contributing to guideline
812 development. Association of Breast Surgery, Member of the clinical practice and standards
813 committee. 3. Receipt of Equipment, Materials, etc.: SECA provided equipment for measuring body
814 composition to University Hospital Southampton under a model industry collaborative agreement.

815

816 **References**

817 1. Conduit, P.T., Wainman, A. & Raff, J.W. Centrosome function and assembly in animal cells.
818 *Nat Rev Mol Cell Biol* **16**, 611-624 (2015).
819 2. Kim, S. & Dynlacht, B.D. Assembling a primary cilium. *Curr Opin Cell Biol* **25**, 506-511
820 (2013).
821 3. Godinho, S.A. & Basto, R. Centrosomes and cancer: balancing tumor-promoting and
822 inhibitory roles. *Trends Cell Biol* **35**, 515-526 (2025).
823 4. Kiermaier, E., Stotzel, I., Schapfl, M.A. & Villunger, A. Amplified centrosomes-more than just
824 a threat. *EMBO Rep* **25**, 4153-4167 (2024).
825 5. Nigg, E.A., Schnerch, D. & Ganier, O. Impact of Centrosome Aberrations on Chromosome
826 Segregation and Tissue Architecture in Cancer. *Cold Spring Harb Symp Quant Biol* **82**,
827 137-144 (2017).
828 6. Raff, J.W. & Basto, R. Centrosome Amplification and Cancer: A Question of Sufficiency.
829 *Dev Cell* **40**, 217-218 (2017).
830 7. Mittal, K. *et al.* Centrosome amplification: a quantifiable cancer cell trait with prognostic
831 value in solid malignancies. *Cancer Metastasis Rev* **40**, 319-339 (2021).
832 8. Boveri, T. Concerning the origin of malignant tumours by Theodor Boveri. Translated and
833 annotated by Henry Harris. *J Cell Sci* **121 Suppl 1**, 1-84 (2008).
834 9. Godinho, S.A. & Pellman, D. Causes and consequences of centrosome abnormalities in
835 cancer. *Philos Trans R Soc Lond B Biol Sci* **369** (2014).
836 10. Hsu, L.C., Kapali, M., DeLoia, J.A. & Gallion, H.H. Centrosome abnormalities in ovarian
837 cancer. *Int J Cancer* **113**, 746-751 (2005).
838 11. Lingle, W.L., Lutz, W.H., Ingle, J.N., Maihle, N.J. & Salisbury, J.L. Centrosome hypertrophy
839 in human breast tumors: implications for genomic stability and cell polarity. *Proc Natl Acad*
840 *Sci U S A* **95**, 2950-2955 (1998).
841 12. Pihan, G.A. *et al.* Centrosome defects and genetic instability in malignant tumors. *Cancer*
842 *Res* **58**, 3974-3985 (1998).
843 13. Sato, N. *et al.* Centrosome abnormalities in pancreatic ductal carcinoma. *Clin Cancer Res*
844 **5**, 963-970 (1999).
845 14. Giehl, M. *et al.* Centrosome aberrations in chronic myeloid leukemia correlate with stage of
846 disease and chromosomal instability. *Leukemia* **19**, 1192-1197 (2005).
847 15. Kramer, A., Neben, K. & Ho, A.D. Centrosome aberrations in hematological malignancies.
848 *Cell Biol Int* **29**, 375-383 (2005).
849 16. Basto, R. *et al.* Centrosome amplification can initiate tumorigenesis in flies. *Cell* **133**, 1032-
850 1042 (2008).
851 17. Lingle, W.L. *et al.* Centrosome amplification drives chromosomal instability in breast tumor
852 development. *Proc Natl Acad Sci U S A* **99**, 1978-1983 (2002).
853 18. Levine, M.S. *et al.* Centrosome Amplification Is Sufficient to Promote Spontaneous
854 Tumorigenesis in Mammals. *Dev Cell* **40**, 313-322 e315 (2017).
855 19. Chan, J.Y. A clinical overview of centrosome amplification in human cancers. *Int J Biol Sci*
856 **7**, 1122-1144 (2011).
857 20. Shekhar, M.P., Lyakhovich, A., Visscher, D.W., Heng, H. & Kondrat, N. Rad6
858 overexpression induces multinucleation, centrosome amplification, abnormal mitosis,
859 aneuploidy, and transformation. *Cancer Res* **62**, 2115-2124 (2002).
860 21. Meraldi, P., Honda, R. & Nigg, E.A. Aurora-A overexpression reveals tetraploidization as a
861 major route to centrosome amplification in p53-/- cells. *EMBO J* **21**, 483-492 (2002).
862 22. Fujiwara, T. *et al.* Cytokinesis failure generating tetraploids promotes tumorigenesis in p53-
863 null cells. *Nature* **437**, 1043-1047 (2005).
864 23. Duensing, A., Chin, A., Wang, L., Kuan, S.F. & Duensing, S. Analysis of centrosome
865 overduplication in correlation to cell division errors in high-risk human papillomavirus
866 (HPV)-associated anal neoplasms. *Virology* **372**, 157-164 (2008).

24. Duelli, D.M., Hearn, S., Myers, M.P. & Lazebnik, Y. A primate virus generates transformed human cells by fusion. *J Cell Biol* **171**, 493-503 (2005).
25. Khodjakov, A. *et al.* De novo formation of centrosomes in vertebrate cells arrested during S phase. *J Cell Biol* **158**, 1171-1181 (2002).
26. La Terra, S. *et al.* The de novo centriole assembly pathway in HeLa cells: cell cycle progression and centriole assembly/maturation. *J Cell Biol* **168**, 713-722 (2005).
27. Davoli, T. & de Lange, T. Telomere-driven tetraploidization occurs in human cells undergoing crisis and promotes transformation of mouse cells. *Cancer Cell* **21**, 765-776 (2012).
28. Borel, F., Lohez, O.D., Lacroix, F.B. & Margolis, R.L. Multiple centrosomes arise from tetraploidy checkpoint failure and mitotic centrosome clusters in p53 and RB pocket protein-compromised cells. *Proc Natl Acad Sci U S A* **99**, 9819-9824 (2002).
29. Karakaya, K. *et al.* Overexpression of EVI1 interferes with cytokinesis and leads to accumulation of cells with supernumerary centrosomes in G0/1 phase. *Cell Cycle* **11**, 3492-3503 (2012).
30. Dwivedi, D., Harry, D. & Meraldi, P. Mild replication stress causes premature centriole disengagement via a sub-critical Plk1 activity under the control of ATR-Chk1. *Nat Commun* **14**, 6088 (2023).
31. Loncarek, J., Hergert, P. & Khodjakov, A. Centriole reduplication during prolonged interphase requires procentriole maturation governed by Plk1. *Curr Biol* **20**, 1277-1282 (2010).
32. Difilippantonio, M.J. *et al.* Nucleation capacity and presence of centrioles define a distinct category of centrosome abnormalities that induces multipolar mitoses in cancer cells. *Environ Mol Mutagen* **50**, 672-696 (2009).
33. Hut, H.M. *et al.* Centrosomes split in the presence of impaired DNA integrity during mitosis. *Mol Biol Cell* **14**, 1993-2004 (2003).
34. Loffler, H., Fechter, A., Liu, F.Y., Poppelreuther, S. & Kramer, A. DNA damage-induced centrosome amplification occurs via excessive formation of centriolar satellites. *Oncogene* **32**, 2963-2972 (2013).
35. Loncarek, J., Hergert, P., Magidson, V. & Khodjakov, A. Control of daughter centriole formation by the pericentriolar material. *Nat Cell Biol* **10**, 322-328 (2008).
36. Starita, L.M. *et al.* BRCA1-dependent ubiquitination of gamma-tubulin regulates centrosome number. *Mol Cell Biol* **24**, 8457-8466 (2004).
37. Marteil, G. *et al.* Over-elongation of centrioles in cancer promotes centriole amplification and chromosome missegregation. *Nat Commun* **9**, 1258 (2018).
38. Tang, C.J., Fu, R.H., Wu, K.S., Hsu, W.B. & Tang, T.K. CPAP is a cell-cycle regulated protein that controls centriole length. *Nat Cell Biol* **11**, 825-831 (2009).
39. Schmidt, T.I. *et al.* Control of centriole length by CPAP and CP110. *Curr Biol* **19**, 1005-1011 (2009).
40. Burgy, L. *et al.* CenFind: a deep-learning pipeline for efficient centriole detection in microscopy datasets. *BMC Bioinformatics* **24**, 120 (2023).
41. Sankaran, D.G., Stemm-Wolf, A.J., McCurdy, B.L., Hariharan, B. & Pearson, C.G. A semi-automated machine learning-aided approach to quantitative analysis of centrosomes and microtubule organization. *J Cell Sci* **133** (2020).
42. Patel, N. *et al.* Integrated genomics and functional validation identifies malignant cell specific dependencies in triple negative breast cancer. *Nat Commun* **9**, 1044 (2018).
43. Mittal, K. *et al.* A Quantitative Centrosomal Amplification Score Predicts Local Recurrence of Ductal Carcinoma In Situ. *Clin Cancer Res* **26**, 2898-2907 (2020).
44. Sauer, C.M. *et al.* Molecular landscape and functional characterization of centrosome amplification in ovarian cancer. *Nat Commun* **14**, 6505 (2023).
45. Khanam, R. & Hussain, M. YOLOv11: An Overview of the Key Architectural Enhancements. *arXiv e-prints*, arXiv:2410.17725 (2024).

46. Ronneberger, O., Fischer, P. & Brox, T. in Medical Image Computing and Computer-Assisted Intervention – MICCAI 2015. (eds. N. Navab, J. Hornegger, W.M. Wells & A.F. Frangi) 234-241 (Springer International Publishing, Cham; 2015).
47. Schmidt, U., Weigert, M., Broaddus, C. & Myers, G. in Medical Image Computing and Computer Assisted Intervention – MICCAI 2018. (eds. A.F. Frangi, J.A. Schnabel, C. Davatzikos, C. Alberola-López & G. Fichtinger) 265-273 (Springer International Publishing, Cham; 2018).
48. Badrinarayanan, V., Kendall, A. & Cipolla, R. SegNet: A Deep Convolutional Encoder-Decoder Architecture for Image Segmentation. *IEEE Transactions on Pattern Analysis and Machine Intelligence* **39**, 2481-2495 (2017).
49. Chen, L.-C., Zhu, Y., Papandreou, G., Schroff, F. & Adam, H. arXiv:1802.02611 (2018).
50. He, L., Zhou, Y., Liu, L., Zhang, Y. & Ma, J. Application of the YOLOv11-seg algorithm for AI-based landslide detection and recognition. *Sci Rep* **15**, 12421 (2025).
51. Sridharan, D.M., Enerio, S., LaBarge, M.A., Stampfer, M.M. & Pluth, J.M. Lesion complexity drives age related cancer susceptibility in human mammary epithelial cells. *Aging (Albany NY)* **9**, 665-686 (2017).
52. Shimomura, A., Miyoshi, Y., Taguchi, T., Tamaki, Y. & Noguchi, S. Association of loss of BRCA1 expression with centrosome aberration in human breast cancer. *Journal of Cancer Research and Clinical Oncology* **135**, 421-430 (2009).
53. Agnoletto, A. & Brisken, C. Hormone Signaling in Breast Development and Cancer, in *A Guide to Breast Cancer Research: From Cellular Heterogeneity and Molecular Mechanisms to Therapy*. (eds. T. Sørlie & R.B. Clarke) 279-307 (Springer Nature Switzerland, Cham; 2025).
54. Loibl, S., Poortmans, P., Morrow, M., Denkert, C. & Curigliano, G. Breast cancer. *The Lancet* **397**, 1750-1769 (2021).
55. Menarche, menopause, and breast cancer risk: individual participant meta-analysis, including 118 964 women with breast cancer from 117 epidemiological studies. *The Lancet Oncology* **13**, 1141-1151 (2012).
56. Type and timing of menopausal hormone therapy and breast cancer risk: individual participant meta-analysis of the worldwide epidemiological evidence. *The Lancet* **394**, 1159-1168 (2019).
57. Heer, E. *et al.* Global burden and trends in premenopausal and postmenopausal breast cancer: a population-based study. *The Lancet Global Health* **8**, e1027-e1037 (2020).
58. Delaval, B. & Doxsey, S.J. Pericentrin in cellular function and disease. *J Cell Biol* **188**, 181-190 (2010).
59. Jiang, T. *et al.* Drivers of centrosome abnormalities: Senescence progression and tumor immune escape. *Semin Cancer Biol* **110**, 56-64 (2025).
60. Nigg, E.A. & Raff, J.W. Centrioles, centrosomes, and cilia in health and disease. *Cell* **139**, 663-678 (2009).
61. Denu, R.A. *et al.* Centrosome amplification induces high grade features and is prognostic of worse outcomes in breast cancer. *BMC Cancer* **16**, 47 (2016).
62. Van Herck, Y. *et al.* Is cancer biology different in older patients? *The Lancet Healthy Longevity* **2**, e663-e677 (2021).
63. Benz, C.C. Impact of aging on the biology of breast cancer. *Critical Reviews in Oncology/Hematology* **66**, 65-74 (2008).
64. Lopes, C.A.M. *et al.* Centrosome amplification arises before neoplasia and increases upon p53 loss in tumorigenesis. *J Cell Biol* **217**, 2353-2363 (2018).
65. Monteiro, P., Yeon, B., Wallis, S.S. & Godinho, S.A. Centrosome amplification fine tunes tubulin acetylation to differentially control intracellular organization. *EMBO J* **42**, e112812 (2023).
66. Godinho, S.A. *et al.* Oncogene-like induction of cellular invasion from centrosome amplification. *Nature* **510**, 167-171 (2014).

971 67. LoMastro, G.M. & Holland, A.J. The Emerging Link between Centrosome Aberrations and
972 Metastasis. *Dev Cell* **49**, 325-331 (2019).
973 68. Rhys, A.D. *et al.* Loss of E-cadherin provides tolerance to centrosome amplification in
974 epithelial cancer cells. *J Cell Biol* **217**, 195-209 (2018).
975 69. Ganier, O. *et al.* Structural centrosome aberrations promote non-cell-autonomous
976 invasiveness. *EMBO J* **37** (2018).
977 70. Garcia-Carpio, I. *et al.* Extra centrosomes induce PIDD1-mediated inflammation and
978 immunosurveillance. *EMBO J* **42**, e113510 (2023).
979 71. Ganier, O., Schnerch, D. & Nigg, E.A. Structural centrosome aberrations sensitize polarized
980 epithelia to basal cell extrusion. *Open Biol* **8** (2018).
981 72. Kahl, I. *et al.* The cell cycle-related genes RHAMM, AURKA, TPX2, PLK1, and PLK4 are
982 associated with the poor prognosis of breast cancer patients. *J Cell Biochem* **123**, 581-600
983 (2022).
984 73. Toft, D.J. & Cryns, V.L. Minireview: Basal-like breast cancer: from molecular profiles to
985 targeted therapies. *Mol Endocrinol* **25**, 199-211 (2011).
986 74. Cosenza, M.R. *et al.* Asymmetric Centriole Numbers at Spindle Poles Cause Chromosome
987 Missegregation in Cancer. *Cell Rep* **20**, 1906-1920 (2017).
988 75. Ganem, N.J., Godinho, S.A. & Pellman, D. A mechanism linking extra centrosomes to
989 chromosomal instability. *Nature* **460**, 278-282 (2009).
990 76. Ingebriktsen, L.M. *et al.* Elevated expression of Aurora-A/AURKA in breast cancer
991 associates with younger age and aggressive features. *Breast Cancer Res* **26**, 126 (2024).
992 77. Wong, Y.L. *et al.* Cell biology. Reversible centriole depletion with an inhibitor of Polo-like
993 kinase 4. *Science* **348**, 1155-1160 (2015).
994 78. Melichar, B. *et al.* Safety and activity of alisertib, an investigational aurora kinase A inhibitor,
995 in patients with breast cancer, small-cell lung cancer, non-small-cell lung cancer, head and
996 neck squamous-cell carcinoma, and gastro-oesophageal adenocarcinoma: a five-arm
997 phase 2 study. *Lancet Oncol* **16**, 395-405 (2015).
998 79. Borisa, A.C. & Bhatt, H.G. A comprehensive review on Aurora kinase: Small molecule
999 inhibitors and clinical trial studies. *Eur J Med Chem* **140**, 1-19 (2017).
1000 80. Veitch, Z.W. *et al.* Safety and tolerability of CFI-400945, a first-in-class, selective PLK4
1001 inhibitor in advanced solid tumours: a phase 1 dose-escalation trial. *Br J Cancer* **121**, 318-
1002 324 (2019).
1003 81. Lei, Q. *et al.* YLT-11, a novel PLK4 inhibitor, inhibits human breast cancer growth via
1004 inducing maladjusted centriole duplication and mitotic defect. *Cell Death Dis* **9**, 1066
1005 (2018).
1006 82. Watts, C.A. *et al.* Design, synthesis, and biological evaluation of an allosteric inhibitor of
1007 HSET that targets cancer cells with supernumerary centrosomes. *Chem Biol* **20**, 1399-1410
1008 (2013).
1009 83. Blyth, R.R.R. *et al.* Development and characterisation of a novel 3D in vitro model of
1010 obesity-associated breast cancer as a tool for drug testing. *NPJ Breast Cancer* **11**, 50
1011 (2025).
1012 84. Daly, A. *et al.* Assessment of body composition in breast cancer patients: concordance
1013 between transverse computed tomography analysis at the fourth thoracic and third lumbar
1014 vertebrae. *Front Nutr* **11**, 1366768 (2024).
1015 85. Bosy-Westphal, A. *et al.* What makes a BIA equation unique? Validity of eight-electrode
1016 multifrequency BIA to estimate body composition in a healthy adult population. *Eur J Clin*
1017 *Nutr* **67 Suppl 1**, S14-21 (2013).
1018 86. Rovero, S. *et al.* DNA vaccination against rat her-2/Neu p185 more effectively inhibits
1019 carcinogenesis than transplantable carcinomas in transgenic BALB/c mice. *J Immunol* **165**,
1020 5133-5142 (2000).
1021 87. Rakha, E.A. *et al.* UK recommendations for HER2 assessment in breast cancer: an update.
1022 *J Clin Pathol* **76**, 217-227 (2023).

88. Ellis, I.O., Rakha, E.A., Tse, G.M. & Tan, P.H. An international unified approach to reporting and grading invasive breast cancer. An overview of the International Collaboration on Cancer Reporting (ICCR) initiative. *Histopathology* **82**, 189-197 (2023).
89. Schindelin, J. *et al.* Fiji: an open-source platform for biological-image analysis. *Nat Methods* **9**, 676-682 (2012).
90. Bankhead, P. *et al.* QuPath: Open source software for digital pathology image analysis. *Sci Rep* **7**, 16878 (2017).
91. Stringer, C. & Pachitariu, M. Cellpose3: one-click image restoration for improved cellular segmentation. *Nat Methods* **22**, 592-599 (2025).
92. Stringer, C., Wang, T., Michaelos, M. & Pachitariu, M. Cellpose: a generalist algorithm for cellular segmentation. *Nat Methods* **18**, 100-106 (2021).
93. Ong, H.T. *et al.* Digitalized organoids: integrated pipeline for high-speed 3D analysis of organoid structures using multilevel segmentation and cellular topology. *Nature Methods* **22**, 1343-1354 (2025).

Fig. 1

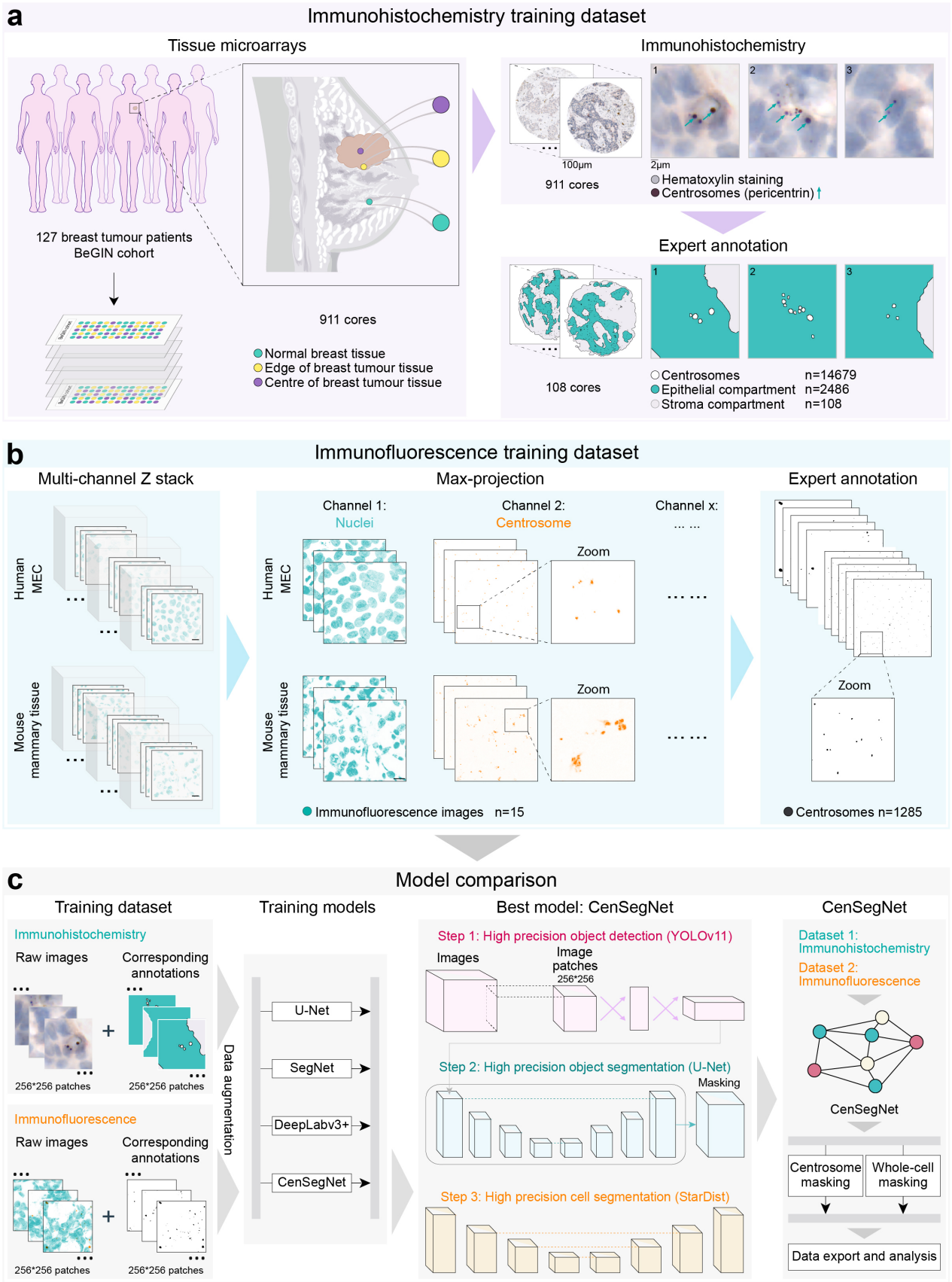
a
Immunohistochemistry training dataset
Tissue microarrays
127 breast tumour patients
BeGIN cohort
911 cores
Normal breast tissue
Edge of breast tumour tissue
Centre of breast tumour tissue
Immunohistochemistry
100µm
2µm
911 cores
Hematoxylin staining
Centrosomes (pericentrin)
Expert annotation
108 cores
Centrosomes n=14679
Epithelial compartment n=2486
Stroma compartment n=108
b
Immunofluorescence training dataset
Multi-channel Z stack
Human MEC
Mouse mammary tissue
Max-projection
Channel 1: Nuclei
Channel 2: Centrosome
Channel x: ... ...
Zoom
Immunofluorescence images n=15
Expert annotation
Centrosomes n=1285
c
Model comparison
Training dataset
Immunohistochemistry
Raw images
Corresponding annotations
256*256 patches
Immunofluorescence
Data augmentation
Training models
U-Net
SegNet
DeepLabv3+
CenSegNet
Best model: CenSegNet
Step 1: High precision object detection (YOLOv11)
Images
Image patches 256*256
Step 2: High precision object segmentation (U-Net)
Masking
Step 3: High precision cell segmentation (StarDist)
CenSegNet
Dataset 1: Immunohistochemistry
Dataset 2: Immunofluorescence
Centrosome masking
Whole-cell masking
Data export and analysis

Fig. 1 Development and benchmarking of CenSegNet for centrosome segmentation. a Left: workflow for generating tissue microarrays (TMAs) comprising 911 breast tissue sample cores from normal breast tissue, breast tumours, and adjacent non-tumour tissue, collected from 127 breast cancer patients in the BeGIN cohort. Figure 1a is schematic for illustrative purposes to demonstrate sampling strategy for the TMA. Cores were taken from FFPE blocks following breast cancer surgery. Top right: immunohistochemical staining of all ROIs with pericentrin (centrosome marker) and haematoxylin (nuclear counterstain). Bottom right: random selection of 108 ROIs used to construct a training dataset containing 2,486 epithelial compartments, 108 stromal compartments and 14,679 annotated centrosomes. **b** Left and middle: representative confocal images of human mammary epithelial cells (MECs) and mouse mammary tumour tissues exhibiting normal or amplified centrosomes. Cells and tissues were stained for pericentrin (orange) and counterstained with DAPI (DNA, teal). Scale bars, 10 μm. Right: training dataset derived from these images, comprising 1,285 annotated centrosomes. **c** Left: 256 × 256 pixel cropped patches from immunohistochemistry and immunofluorescence datasets. Middle left: training of existing segmentation architectures (U-Net, SegNet, DeepLabv3+) and the proposed CenSegNet using these datasets. Middle right: CenSegNet performance across both immunohistochemistry and immunofluorescence test sets. CenSegNet operates in three sequential phases: (1) object detection to generate bounding-box predictions for individual centrosomes; (2) pixel-level segmentation of detected objects; (3) StarDist-based whole-cell segmentation.

Fig. 2

a

Performance of published models *versus* CenSegNet

Raw images | U-Net | SegNet | DeepLabv3+ | CenSegNet (ours)

Ground-truth | Prediction | Overlap

Immunohistochemistry
DNA Centrosomes

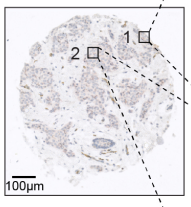

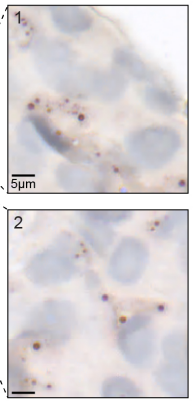

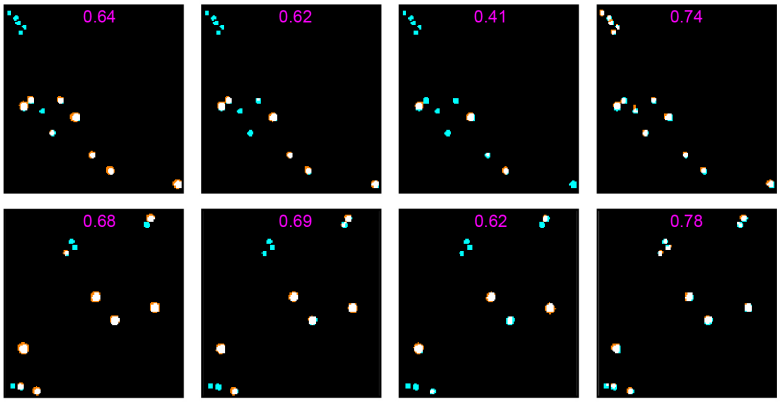

Immunofluorescence
DNA Centrosomes

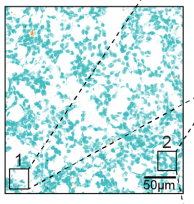

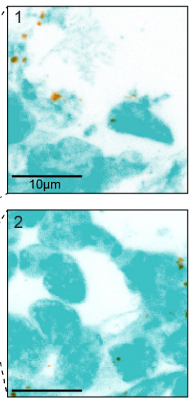

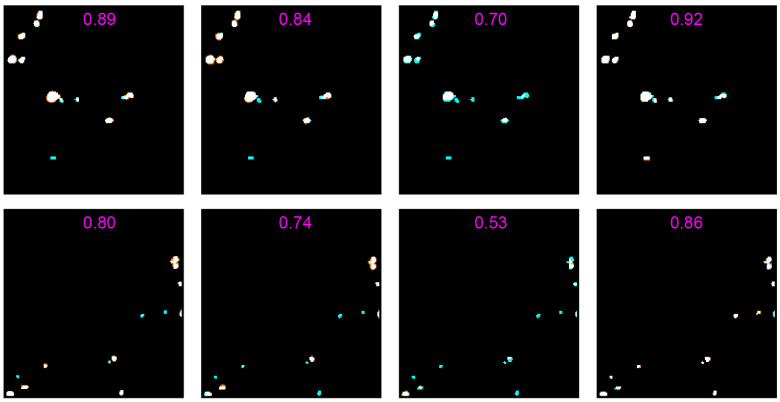

b

Immunohistochemistry
R^2=0.9999; p<0.0001

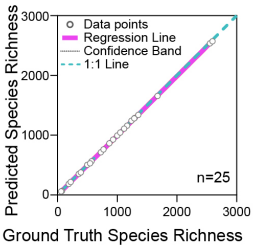

c

Immunofluorescence
R^2=0.9873; p<0.0001

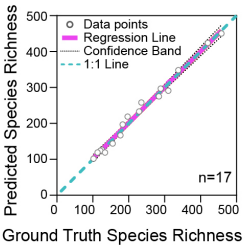

Detection efficiency

d

Immunohistochemistry
R^2=0.9613; p<0.0001

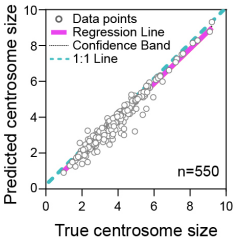

e

Overall F1 score (0.82) of Immunohistochemistry and Immunofluorescence datasets

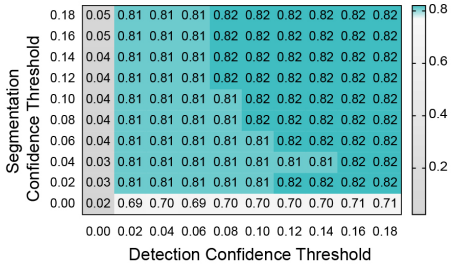

Segmentation efficiency

f

Annotated 6,475 centrosomes in testing dataset

	0.0 to 0.5	0.5 to 1.0	1.0 to 1.5	1.5 to 2.0	2.0 to 2.5	2.5 to 3.0	3.0 to 3.5	3.5 to 4.0	4.0 to 4.5	4.5 to 5.0	5.0 to 5.5	5.5 to 6.0	6.0 to 6.5	6.5 to 7.0	7.0 to 7.5	7.5 to 8.0	8.0 to 8.5	8.5 to 9.0	9.0 to 9.5	9.5 to 10.0	10.0 to 10.5	>10.5
Normal	0.760	2.172	14.549	23.779	19.870	14.115	8.903	6.515	3.800	2.172	1.846	0.977	0.543	0	0	0	0	0	0	0	0	0
Edge	0.742	1.002	6.496	14.551	20.490	18.560	13.215	9.725	5.457	4.269	1.856	1.411	0.965	0.371	0.148	0.186	0.111	0.186	0.074	0.074	0.074	0.037
Tumour	0.769	1.993	10.245	13.951	22.343	21.259	13.741	8.042	3.916	1.748	1.294	0.315	0.105	0.245	0.035	0	0	0	0	0	0	0

Percentage (0, 10, 20, 30)

μm²

g

Segmented 333,148 centrosomes in testing dataset

	0.0 to 0.5	0.5 to 1.0	1.0 to 1.5	1.5 to 2.0	2.0 to 2.5	2.5 to 3.0	3.0 to 3.5	3.5 to 4.0	4.0 to 4.5	4.5 to 5.0	5.0 to 5.5	5.5 to 6.0	6.0 to 6.5	6.5 to 7.0	7.0 to 7.5	7.5 to 8.0	8.0 to 8.5	8.5 to 9.0	9.0 to 9.5	9.5 to 10.0	10.0 to 10.5	10.5 to 11.0	11.0 to 11.5	11.5 to 12.0	>12.0
Normal	0.849	2.151	10.947	16.301	23.232	21.303	10.652	6.424	3.720	1.975	1.237	0.785	0.425	0	0	0	0	0	0	0	0	0	0	0	0
Edge	0.726	1.962	8.090	14.750	22.430	21.719	12.500	7.743	4.754	2.363	1.240	0.812	0.431	0.192	0.108	0.063	0.037	0.037	0.009	0.013	0.009	0.003	0.005	0.003	0.004
Tumour	0.826	2.521	10.742	16.126	21.652	20.663	11.787	7.082	4.260	1.974	1.088	0.625	0.279	0.158	0.092	0.049	0.030	0.020	0.011	0.006	0.004	0.001	0.002	0.002	0.003

Fig. 2 Validation of CenSegNet performance against alternative models and human annotations. a Left: representative immunohistochemistry and immunofluorescence images used for centrosome segmentation. Right: colour overlays showing predictions from U-Net, SegNet, DeepLabv3+, and CenSegNet (teal: ground-truth annotations; orange: predicted segmentation; white: overlap between predictions and ground-truth). Magenta text indicates the F1 score for corresponding images of each method (0: complete disagreement; 1: complete concordance). Yellow arrow marks the overprediction. **b** Pearson correlation between centrosome counts predicted by CenSegNet and ground truth across 25 immunohistochemistry images. Grey circles represent individual patients, purple line represents regression line, Black dot line represents confidence band, and teal dot line represents 1:1 line. Two-tailed Pearson correlation test followed by simple linear regression for visualisation, ****$P < 0.0001$. **c** Pearson correlation between centrosome counts predicted by CenSegNet and ground truth across 17 immunofluorescence images. Two-tailed Pearson correlation test, followed by simple linear regression for graphical representation, ****$P < 0.0001$. **d** Pearson correlation between centrosome size predicted by CenSegNet and measured by annotators (n = 550 centrosomes from >200 ROIs across 20 images). Two-tailed Pearson correlation test, followed by simple linear regression for graphical representation, ****$P < 0.0001$. **e** Heatmap of overall F1 scores (maximum 0.82) from combined immunohistochemistry and immunofluorescence test datasets. The *x*-axis represents the detection confidence threshold, and the *y*-axis represents the segmentation confidence threshold. Each cell represents the mean F1 score for that threshold pair; darker cyan indicates higher values. Optimal performance (F1 = 0.82) was achieved across a broad range of threshold combinations, indicating model robustness to parameter variation. **f, g** Manual annotations of 6,475 centrosomes from normal, edge, and tumour regions—stratified by size (0.5–1.0 μm^2 to >10.5 μm^2) **(f)** were compared with automated segmentations from the full dataset of 333,148 centrosomes **(g)** (0–0.5 μm^2 to >12.0 μm^2). CenSegNet segmentation achieved performance comparable to expert human annotation. Data are presented as individual data points. Source data are provided as Source Data file.

Fig. 3

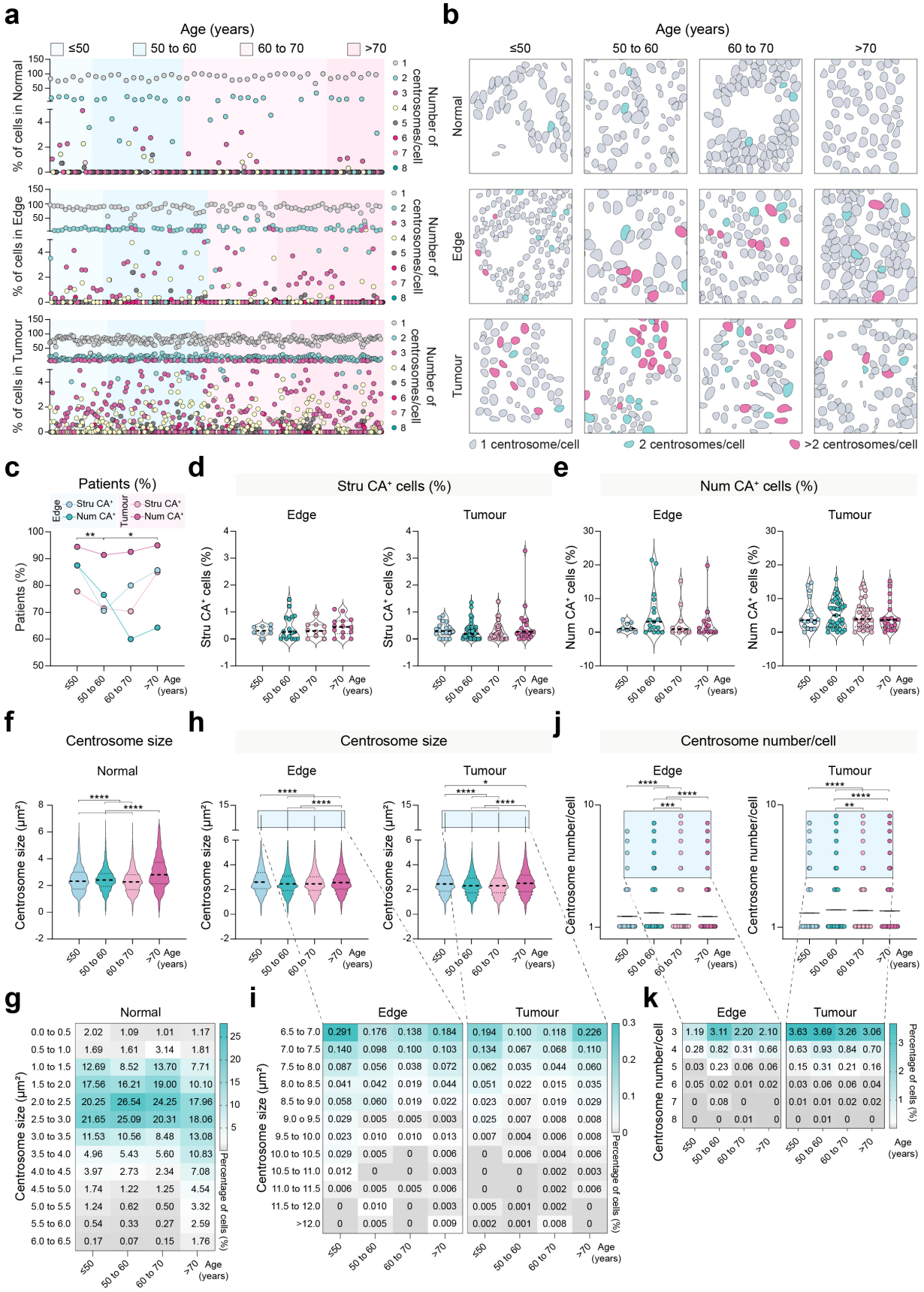
a
Age (years)
≤50
50 to 60
60 to 70
>70
% of cells in Normal
% of cells in Edge
% of cells in Tumour
Number of centrosomes/cell
b
Age (years)
Normal
Edge
Tumour
1 centrosome/cell
2 centrosomes/cell
>2 centrosomes/cell
c
Patients (%)
Stru CA⁺
Num CA⁺
Edge
Tumour
Patients (%)
Age (years)
d
Stru CA⁺ cells (%)
Edge
Tumour
e
Num CA⁺ cells (%)
f
Centrosome size
Normal
Centrosome size (μm²)
h
Centrosome size
j
Centrosome number/cell
g
Normal
Percentage of cells (%)
i
Edge
Tumour
k
Percentage of cells (%)

Fig. 3 Age-related gradients of centrosome aberrations across breast tissue regions. a Percentage of cells with different centrosome numbers in normal, edge, and tumour regions. **b** Representative cell segmentation masks of normal, edge, and tumour regions across patient age groups (Light grey: cells with one centrosome; purple: cells with two centrosomes; cyan: cells with more than two centrosomes). **c** Percentage of patients with structural CA (Stru CA) and Num CA across age groups in edge (≤50 years: n = 8 patients; 50–60 years: n = 17 patients; 60–70 years: n = 10 patients; >70, n = 14 patients) and Tumour (≤50 years: n = 18 patients; 50–60 years: n = 35 patients; 60–70 years: n = 27 patients; >70 years: n = 20 patients) regions. Two-way ANOVA with Tukey's test, $^{*}P = 0.0477$, $^{**}P = 0.0053$. Data are presented as mean ± s.e.m. **d** Percentage of cells with Stru CA in edge and tumour regions across age in Edge and Tumour regions. One-way ANOVA (Stru CA^{+} cells: Edge, $P = 0.7637$; Tumour, $P = 0.4489$ with Tukey's test. absence of asterisks indicates no statistically significant correlation. **e** Percentage of cells with Num CA in edge and tumour regions across age. One-way ANOVA (Num CA^{+} cells: Edge, $P = 0.3427$; Tumour, $P = 0.9086$) with Tukey's test, absence of asterisks indicates no statistical significance. Data are presented as mean ± s.e.m. **f, g** Centrosome segmentation results from normal regions across age groups, stratified by size (0.5–1.0 μm^2 to 6.0–6.5 μm^2). One-way ANOVA ($^{****}P < 0.0001$) with Tukey's test, $^{****}P < 0.0001$. Data are presented as violin plots showing the distribution of values; dashed lines indicate median and interquartile ranges. **h, i** Centrosome segmentation results from edge and tumour regions across age groups, stratified by size (6.5–7.0 μm^2 to 12.0 μm^2). One-way ANOVA ($^{****}P < 0.0001$) with Tukey's test, Edge: $^{****}P < 0.0001$; Tumour: $^{*}P = 0.0484$, $^{****}P < 0.0001$. Data are presented as violin plots showing the distribution of values; dashed lines indicate median and interquartile ranges. **j, k** Centrosome number per cell in edge and tumour regions across age groups, stratified by centrosome number (1–8). One-way ANOVA (Edge, $^{****}P < 0.0001$; Tumour, $^{****}P < 0.0001$) with Tukey's test, Edge: $^{***}P = 0.0006$, $^{****}P < 0.0001$; Tumour: $^{**}P = 0.0054$, $^{****}P < 0.0001$, absence of asterisks indicates no statistical significance. Data are presented as individual data points and mean ± s.e.m. Source data are provided as Source Data file.

Fig. 4

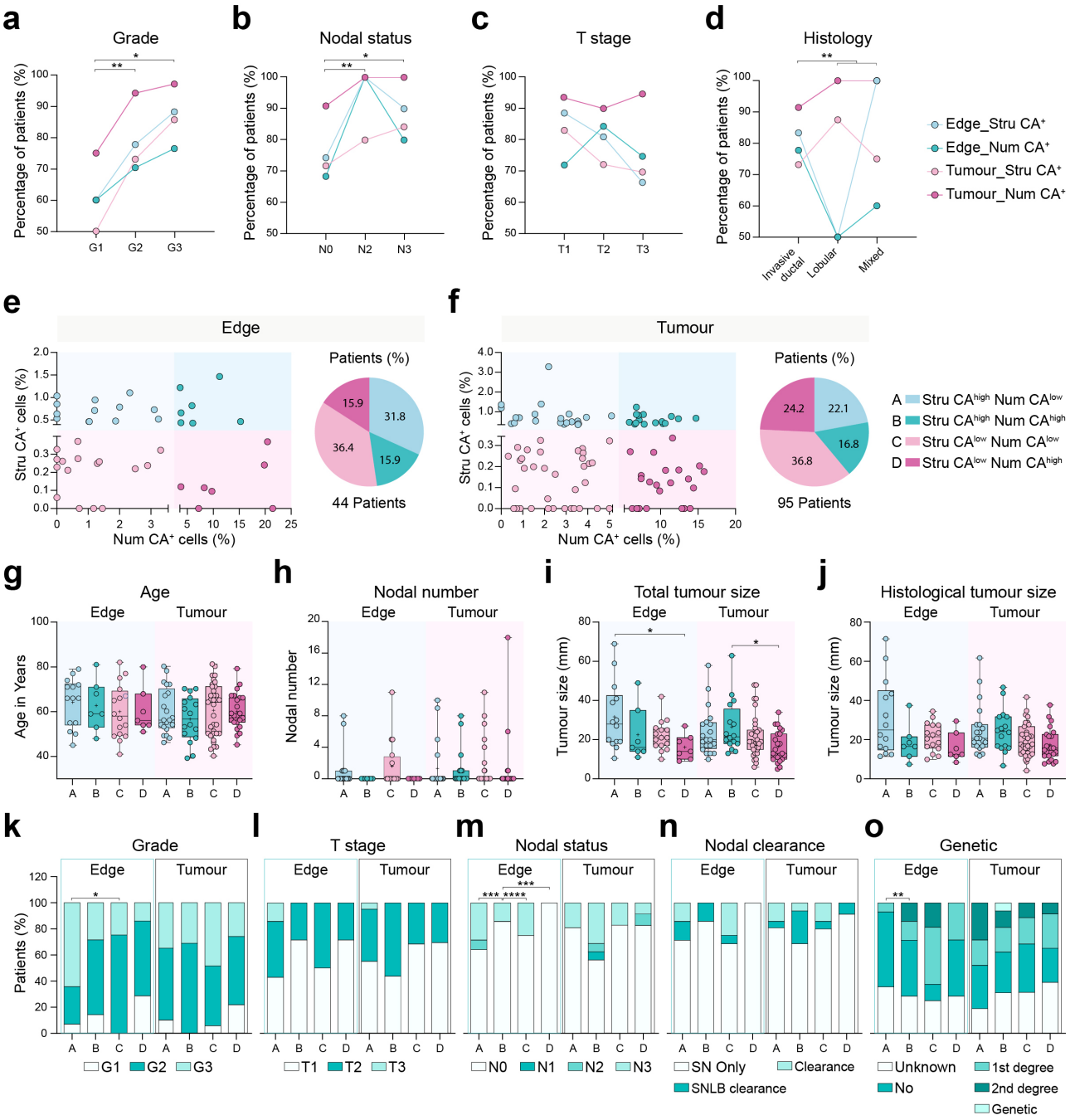

Fig. 4 Patient stratification by CA burden and correlation with clinicopathological features. a–d Percentage of patients with Stru CA and Num CA across histological tumour grade, nodal status, histological tumour size, and histological tumour type in Edge [Grade: G1 (n= 5), G2 (n=27), G3 (n=17); Nodal status: N0 (n=38), N2 (n=1), N3 (n=10); T stage: T1 (n=18), T2 (n=16), T3 (n=15); Histological type: Invasive ductal (n=36), Lobular (n=8), Mixed (n=5)], and Tumour [Grade: G1 (n=12), G2 (n=52), G3 (n=35); Nodal status: N0 (n=77), N2 (n=4), N3 (n=18); T stage: T1 (n= 30), T2 (n= 29), T3 (n= 40); Histological type: Invasive ductal (n=82), Lobular (n=8), Mixed (n=8)] regions. Two-way ANOVA (Grade, $^{**}P = 0.0020$; Nodal status, ** $P = 0.0030$; T stage, $P = 0.4024$; Histological

type, ** P = 0.0037) with Tukey's test, Grade: *P = 0.0130, **P = 0.0018; Nodal status: *P = 0.0113, **P = 0.0030; Histological type: (Invasive ductal *versus* Lobular) **P = 0.0063, (Invasive ductal *versus* Mixed) **P = 0.0061. Data are presented as mean ± s.e.m. **e, f** Patients classified by composite CA burden into $Stru^{high}Num^{low}$ (A), $Stru^{high}Num^{high}$ (B), $Stru^{low}Num^{low}$ (C), and $Stru^{low}Num^{high}$ (D) groups in Edge (A: n = 14 patients; B: n = 7 patients; C: n = 16 patients; D: n = 7 patients) and Tumour (A: n = 20 patients; B: n = 16 patients; C: n = 35 patients; D: n = 23 patients) regions. Histograms and pie charts show percentages of patients in each group in edge and tumour regions. **g–j** Comparative analysis of patient characteristics, including age, number of involved nodes, and total and histological tumour size, across composite CA groups A–D in edge and tumour regions. One-way ANOVA Age (Edge, P = 0.7719; Tumour, P = 0.6469) Nodal number (Edge, P = 0.3164; Tumour, P = 0.9944); Total tumour size (Edge, *P = 0.0491; Tumour, *P = 0.0318); Histological tumour size (Edge, *P = 0.0403; Tumour, P = 0.0732) with Tukey's test, Total tumour size (Edge, *P (A vs D) = 0.0484; Tumour, *P (B vs D) = 0.0296). Absence of asterisks indicates no statistical significance. Data are presented as individual data points and as box and whiskers plots showing the distribution of values, median and quartiles. **k–o** Percentage of patients with different tumour characteristics (histological tumour grade, T stage, nodal status, nodal clearance, genetic subtype) across composite CA groups A–D in edge and tumour regions. Fisher's exact test, left: *P = 0.0261; middle: ***P = 0.0005 (middle left), ***P = 0.0006 (middle right) and ****P < 0.0001; right: **P = 0.0091. **o** 1st degree, family history with 1st degree relative; 2nd degree, family history with 2nd degree relative. Genetic, pathogenic variant in breast cancer-related gene. Source data are provided as Source Data file.

Fig. 5

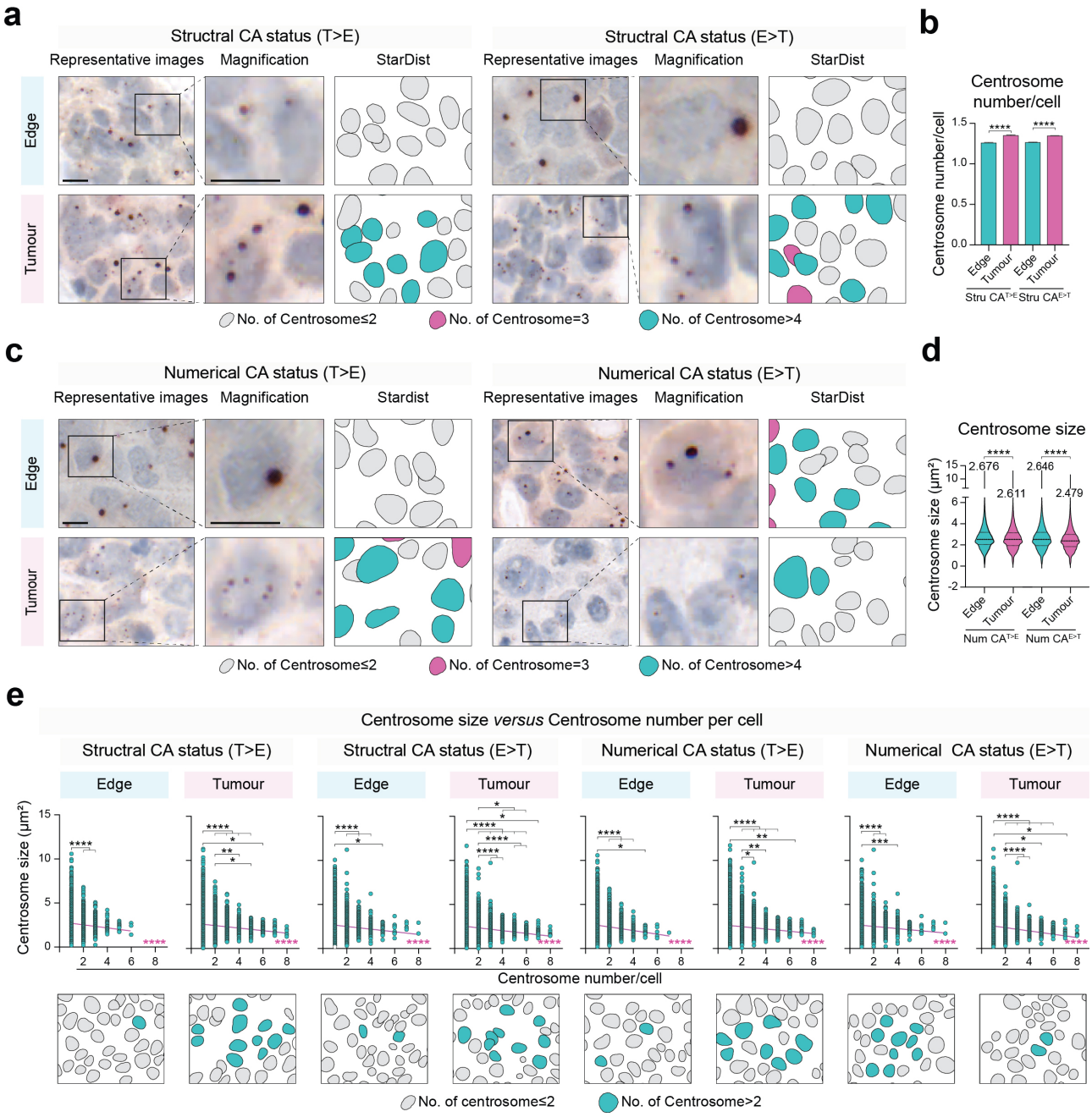

Fig. 5 Interplay between Stru CA and Num CA drives centrosome defect spatial heterogeneity in breast edge and tumour regions. a Representative immunohistochemistry images of human breast tumour tissues (stained for pericentrin, counterstained with haematoxylin) and corresponding StarDist cell masks showing differences in Stru CA between edge and tumour regions. Left: Stru CA higher in Tumour than Edge. Right: Stru CA lower in Tumour than Edge (teal: cells with ≥4 centrosomes; purple: cells with three centrosomes; grey: cells with ≤2 centrosomes). Scale bars, 10 μm. **b** Comparative analysis of centrosome number per cell in edge and tumour regions for Stru $CA^{T>E}$ and Stru $CA^{E>T}$ groups. Comparisons between Edge and Tumour were performed separately for each condition using two-sided unpaired *t*-test, left: ****$P < 0.0001$; right: ****$P < 0.0001$. Data

are presented as mean ± s.e.m. **c** Representative immunohistochemistry images of human breast tumour tissues (stained for pericentrin, counterstained with haematoxylin) and corresponding StarDist cell masks showing differences in Stru CA and Num CA between edge and tumour regions. Left: Num CA higher in Tumour than Edge. Right: Num CA lower in tumour than edge (teal: cells with ≥4 centrosomes; purple: cells with three centrosomes; grey: cells with ≤2 centrosomes). **d** Comparative analysis of centrosome size in Edge and Tumour regions for Num $CA^{T>E}$ and Num $CA^{E>T}$ groups. Comparisons between Edge and Tumour were performed separately for each condition using two-sided unpaired *t*-test. Left: ****$P < 0.0001$; right: ****$P < 0.0001$. Data are presented as violin plots showing the distribution of values; dashed lines indicate median and interquartile ranges. **e** Top: correlation between centrosome number and mean centrosome size at the single-cell level in Stru $CA^{T>E}$, Stru $CA^{E>T}$, Num $CA^{T>E}$, and Num $CA^{E>T}$ groups. One-way ANOVA (****$P < 0.0001$ across Stru $CA^{T>E}$, Stru $CA^{E>T}$, Num $CA^{T>E}$, and Num $CA^{E>T}$ groups) with Tukey's test: Stru $CA^{T>E}$ [Edge: ****$P < 0.0001$; Tumour: (top) *$P = 0.0318$, (bottom) *$P = 0.0416$, **$P = 0.0056$, ****$P < 0.0001$]; Stru $CA^{E>T}$ [Edge: *$P = 0.0139$, ****$P < 0.0001$; Tumour: (top) *P (2 vs 5) = 0.0362, (top) *P (2 vs 6) = 0.0144, ****$P < 0.0001$); Num $CA^{T>E}$ [Edge: *$P = 0.0259$, ****$P < 0.0001$; Tumour: *$P = 0.0421$, (top) **$P = 0.0081$, (bottom) **$P = 0.0025$, ****$P < 0.0001$]; Num $CA^{E>T}$ [Edge: ***$P = 0.0003$, ****$P < 0.0001$; Tumour: (top) *$P = 0.0340$, (bottom) *$P = 0.0115$, ****$P < 0.0001$]. Bottom: Corresponding representative StarDist masks showing cells with Stru CA and Num CA in Edge and Tumour regions. Data are presented as individual data points and mean ± s.e.m. Source data are provided as Source Data file.

Fig. 6

a

```
model = initialize_CenSegNet()
predicted_mask, roi = model. predict (img)
```

b

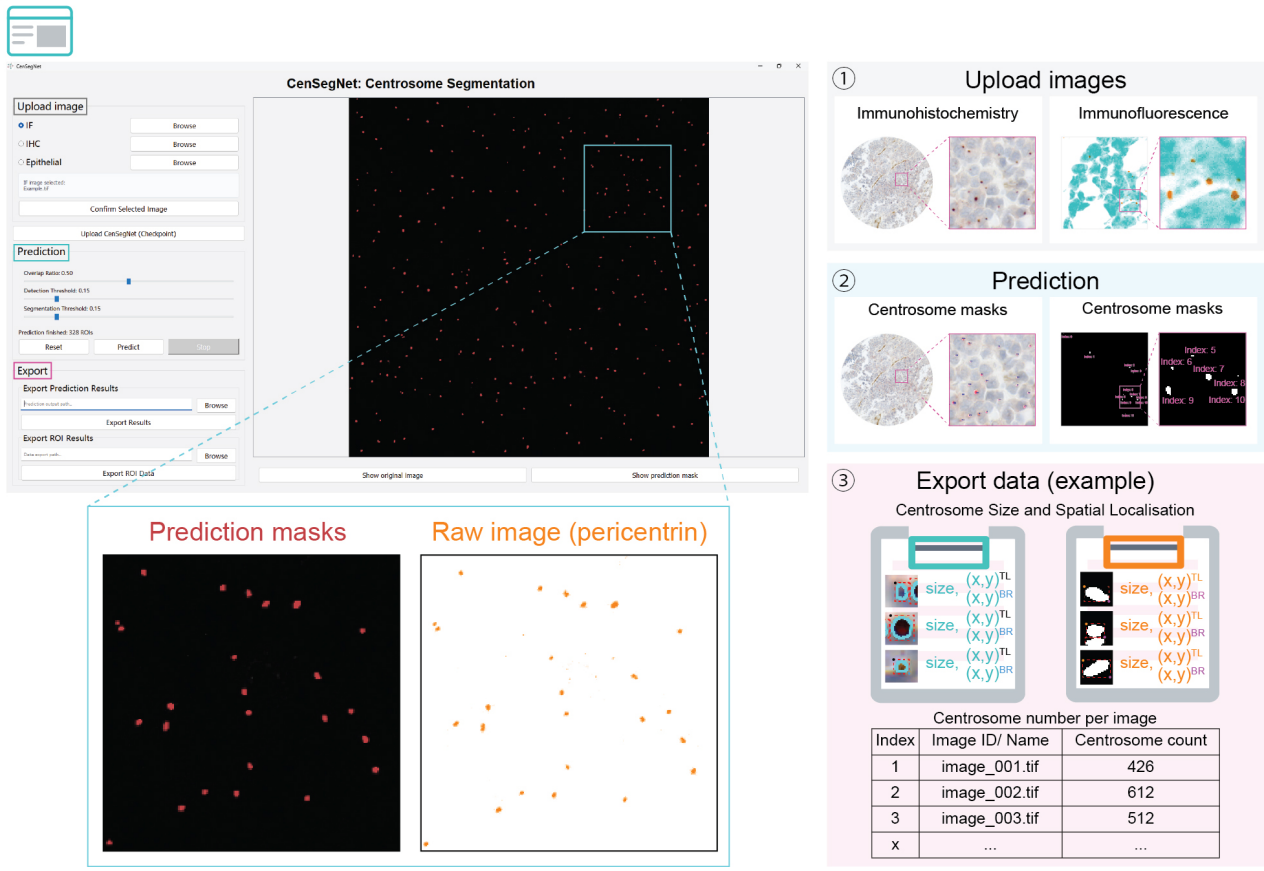

Fig. 6 Open accessibility and integration of CenSegNet for broad adoption. a CenSegNet can be accessed *via* a Python application programming interface (API). **b** Top: graphical user interface (GUI) of CenSegNet designed for a streamlined workflow, supporting image upload, model-based prediction, and data export. Bottom: interface functions for both immunohistochemistry and immunofluorescence images, enabling users to upload images, apply the relevant prediction models, and export quantitative data including pixel-level centrosome size, localisation, and count.